Impact of Structural Coherence and Disorder on the Ionic Transport and Lattice Dynamics in Li$^+$-conducting Argyrodites

Thorben Böger[a,b], Kyra Strotmann[a], Vasiliki Faka[a], Oliver Maus[a,b], Douglas L. Abernathy[c], Garrett E. Granroth[c], Niina H. Jalarvo[c], Cheng Li[c], Emmanuelle Suard[d], Wolfgang G. Zeier*[a,b,e]

[a]Institute of Inorganic and Analytical Chemistry, University of Münster, 48149 Münster, Germany

[b]International Graduate School for Battery Chemistry, Characterization, Analysis, Recycling and Application (BACCARA), University of Münster, 48149 Münster, Germany

[c]Neutron Scattering Division, Oak Ridge National Laboratory, Oak Ridge, 37831, TN, United States

[d]Diffraction group, Institute Laue-Langevin (ILL), 71 avenue des Martyrs, 38000 Grenoble, France

[e]Institute of Energy Materials and Devices (IMD), IMD-4: Helmholtz-Institut Münster: Ionics in Energy Storage, Forschungszentrum Jülich, 48149 Münster, Germany

Corresponding author emails: wzeier@uni-muenster.de

Keywords: lithium argyrodites; thermal conductivity; ionic conductivity; coherence length; inelastic neutron scattering; quasi-elastic neutron scattering; pair-distribution function

Abstract

Solid-state batteries offer improved safety and higher energy density compared to conventional lithium-ion systems. Among candidate solid electrolytes, lithium argyrodites stand out for their exceptional ionic conductivity and compositional flexibility. Recent studies have revealed strongly anharmonic, liquid-like ion and lattice dynamics in these materials, including the collapse of soft phonons driven by Li^+ diffusion, which impacts both local vibrations and thermal transport. Yet, the connection between local structure, phonon dynamics, and macroscopic heat transport remains unresolved. In this work, we employ post-synthesis processing to tune microstructural parameters—such as crystallite size, strain, and coherence length—in two model systems: $Li_{5.5}PS_{4.5}Cl_{1.5}$ and Li_6PS_5Br,. We systematically examine how mechanical treatments influence structural coherence, ion and lattice dynamics, and thermal transport. To further probe the role of structural disorder, we investigate bromide substitution in Li_6PS_5I. Across all compounds, thermal transport above 100 K is dominated by diffusons. At lower temperatures, however, structural disorder is significantly more effective than reduced coherence length at suppressing phonon-gas-type transport, underscoring the crucial role of local structure. Together with a detailed analysis of lithium-ion dynamics, these results provide new insights into how structural coherence and disorder govern both transport and vibrational properties in fast ionic conductors.

Introduction

The ongoing electrification of processes that were previously reliant on fossil fuels has created a growing need for efficient electrical energy storage solutions. Electrochemical energy storage systems in the form of batteries are widely used today, but employ almost exclusively on liquid electrolyte-based electrolytes.[1] In contrast, solid-state batteries utilize a solid electrolyte and promise several potential benefits over traditional lithium-ion batteries.[2] These include enhanced safety and energy density due to the possibility of bipolar stacking[3] and the use of advanced anodes such as silicon (alloy)[4] or even lithium metal[5,6]. A solid electrolyte suited for application in a solid-state battery should possess (kinetic) electrochemical stability against the active materials, high ionic conductivity, and good processibility.[7]

Among the many classes of solid electrolytes, the lithium argyrodite family stands out due to their high ionic conductivity and various possibilities for iso- and aliovalent substitutions.[8] Although orthorhombic and monoclinic low temperature phases exist, the high temperature cubic structure (space group $F\bar{4}3m$, Figure 1a and b) exhibits far superior ionic conductivity, making it the focus of research. To stabilize the cubic polymorph at room temperature, halide ions are typically substituted into the argyrodite structure leading to a general formula of $Li_{7-y}PS_{6-y}X_y$ (X=Cl, Br, I; $0 \leq y \leq 1.5$). In this structure, the halide ions (Wyckoff 4*a*) form a face-centered cubic (fcc) lattice with PS_4^{3-} polyanions occupying the octahedral voids, while “free” sulfide ions fill half of the tetrahedral voids (4*d* position). Both the chloride and bromide ions show anion site disorder with the free sulfide ions.[9] The lithium ions occupy tetrahedrally coordinated sites forming face-sharing polyhedra that create partially occupied cages around the 4*d* position (Figure 1a and b). The occupancy and distribution of lithium ions with respect to the halide ion[9], disorder[10], and amount of halides[11] has been extensively studied in the literature. In short, in $Li_{5.5}PS_{4.5}Cl_{1.5}$ the T2 and T5 positions (both 48*h*) are occupied, whereas in Li_6PS_5Br Li^+ ions are also found to populate the trigonal-planar coordinated T5a positions (24*g* position) at the saddle point in between two T5 positions (Figure 1b). *Intra*-cage diffusion of Li^+ ions can occur via T5-T5a-T5 or T2-T5 jumps. For long-range transport, Li^+ ions need to be able to jump from one cage to another. This *inter*-cage transport takes place via T2-T2 jumps.

Solely by halide substitution ionic conductivities of $\approx 10\ \mathrm{mS \cdot cm^{-1}}$ at room temperature have been achieved.[12,13] The extent to which lattice vibrations influence ionic transport, and whether these vibrations can be systematically tuned to enhance ionic conductivity, is still an open question, not only in lithium argyrodites but in solid electrolytes in general. By using a combination of quasi-elastic neutron scattering (QENS), inelastic neutron scattering (INS), and machine-learned molecular dynamics simulations, Ding et al.[14] recently have shown that upon heating, the phonon dynamics in Li_6PS_5Cl change. With increasing temperature and the fast ion diffusion, the Li^+ sublattice softens and heavily dampens the phonons, indicative of a potential energy surface with significant anharmonicity. Due to the high mobility of Li^+ ions, vibrations associated with Li^+ were found to break down entirely at elevated temperatures, leading to a linear phonon density of states (DOS) $g(\omega)\propto\omega$ at low frequencies ω, instead of the conventional quadratic Debye scaling law $g(\omega)\propto\omega^2$. This altered frequency dependency suggests a liquid-like ion dynamics (Figure 1c) at high temperatures for the low frequency vibrations. Additionally, by selectively restricting the degrees of freedom of specific parts of the host lattice, they reported the host vibrations, especially of PS_4^{3-} tetrahedra, to enhance the Li^+ diffusivity by an order of magnitude over a frozen host lattice. This enhancement is attributed to the "dynamical breathing" of local bottlenecks along the diffusion pathways. It seems that by transitioning from Debye-behavior of vibrations to a more liquid vibrational characteristic, the fast ionic conduction of lithium argyrodites needs to be understood by a Li^+ diffusion in a strong anharmonic regime, suggesting more focus on individual ion vibrations rather than average vibrational frequencies. To further explore the ion dynamics, phononic properties and ultimately thermal transport in lithium argyrodites, this work investigates how coherence length and local vibrations influence their structural and transport properties (Figure 1d).

Measurements of ionic conductivity and electrolyte properties cannot be universally generalized for a given solid electrolyte composition, but are a function of the synthesis method[15], the particle size[16,17], and the structural coherence length[18]. While particle size and coherence length are interrelated concepts, they describe phenomena on vastly different length scales. Particle size refers to the dimensions of secondary solid electrolyte agglomerates, typically in the micrometer range. In contrast, coherence length measures the distance over which atomic order is maintained. Strain and reduced crystallite size diminish the coherence length, and both require harsh mechanical treatment, which in turn also reduces particle size.[18,19] Therefore, smaller coherence length and crystallite size is often accompanied with smaller particle size. The measurement of electrolyte properties as a function of their coherence length gives a measure for the importance of local factors on that property. For example, Maus *et al.*[18] investigated the influence of different post-synthesis treatments on the local structure, ionic conductivity, and battery performance of $Li_{5.5}PS_{4.5}Cl_{1.5}$. It was found that a reduction in coherence length and particle size has opposite effects on the battery performance: a smaller particle size enhances battery performance due to a more uniform interface with the Li metal anode[17], higher interfacial area[16] and reduced tortuosity and in turn higher partial transport[16,18]. In contrast, the loss in coherence length has been reported to cause a reduction in ionic conductivity in $Li_{5.5}PS_{4.5}Cl_{1.5}$, adversely affecting battery performance.[18] Despite the decreasing ionic conductivity, the activation energy E_A remained almost constant suggesting no influence on the total energy landscape.

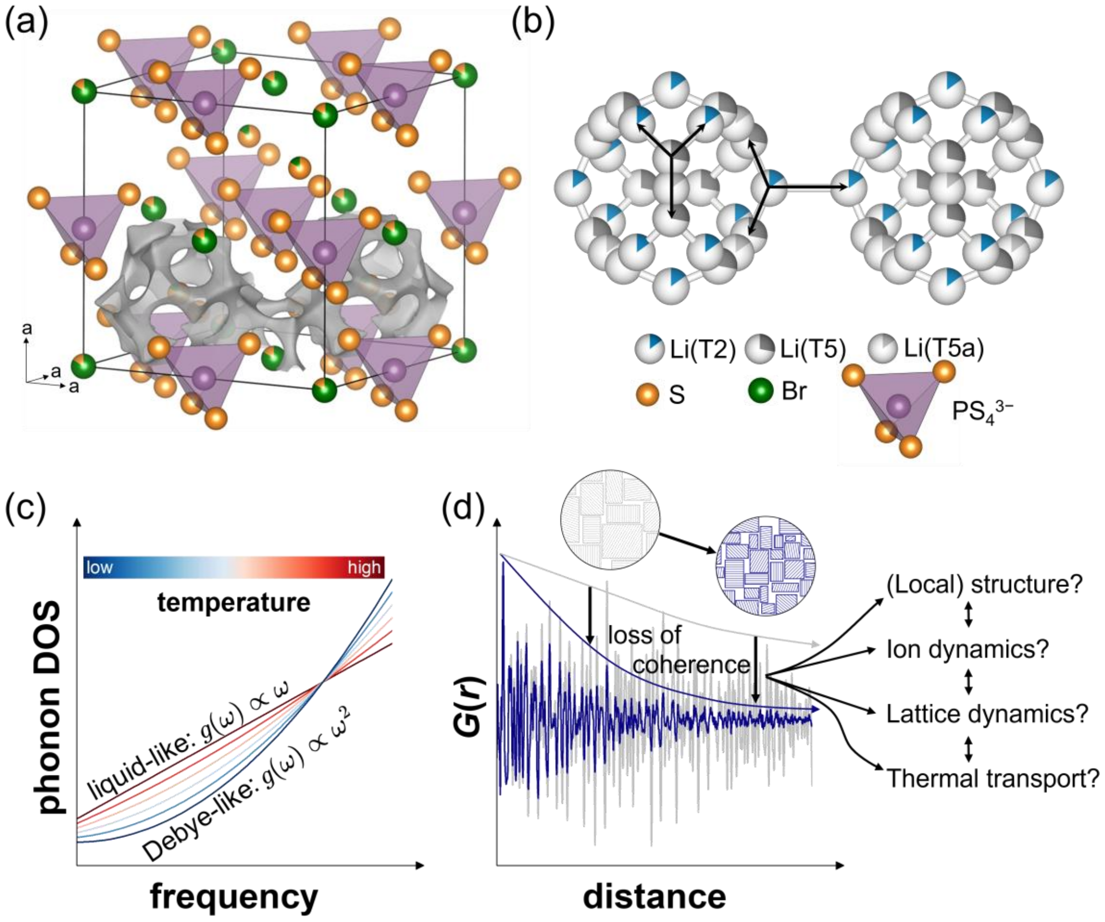

Figure 1. (a) The cubic polymorph of lithium argyrodites, features cages of Li^+ *ions surrounding a sulfide ion. Two of these cages are illustrated via a bond valence sum isosurface (gray). This bond valence*

sum isosurface represents the probability density of lithium ions at elevated temperatures, where the lithium ion sublattice exhibits highly dynamic, liquid-like behavior. (b) Interconnection of Li^+ sites. Intra- and inter-cage jumps are visualized with black arrows. While a T5 site is connected to two T2 sites and another T5 site (via the intermediary T5a site), lithium ions on T2 sites can migrate to two adjacent T5 sites or via an inter-cage jump to another T2 site. (c) Schematic transition from Debye-like to liquid-like phonon DOS upon warming due to the increased mobility of Li^+ ions. At elevated temperatures the diffusion of Li^+ ions leads to a non-zero phonon DOS at a frequency of zero. (d) Mechanical input leads to a loss in coherence seen by a more pronounced decay of the reduced pair distribution function G(r) and schematically shown via exemplary microstructures. The loss of coherence, which is accompanied by smaller crystallite and particle sizes, may affect other quantities including structural properties, lattice as well as ion and thermal transport dynamics. This work aims to elucidate the effect of different processing procedures on such properties.

In addition to a fundamental interest to understand dynamics in solid electrolytes, such investigations are also of practical relevance as the consideration of thermal load in solid-state batteries will become important upon commercialization. Solid-state batteries can present thermal hazards, as for instance, charged Lithium-Nickel-Manganese-Cobalt-Oxide (NCM) in contact with sulfide electrolytes can ignite spontaneously at temperatures as low as 100 °C, even under inert atmospheres.[20] Additionally, while thermal runaway may be avoided, elevated temperatures accelerate decomposition reactions, shortening battery life, whereas low temperatures impair ionic conductivity, reducing capacity and rate performance.[20,21] Studies investigating thermal conductivity of solid electrolytes are scarce, but unanimously report that these materials deviate significantly from the predictions of the phonon gas model traditionally used to describe temperature-dependent thermal conductivity in crystalline solids.[22–24] In this model, lattice vibrations, quantized as bosonic quasiparticles called phonons, propagate through the material until they get scattered. In electronic insulators scattering either occurs at defects, such as mass contrasts due to site disorder or partial occupancy, strain or grain boundaries, or via interactions with other phonons.[25] Characteristic for the phonon gas model is a peak in thermal conductivity at low temperatures (typically below 50 K). At higher temperatures the thermal conductivity is expected to scale with T^{-1}, representing classic Umklapp-scattering.[25] These temperature dependences can be found in most crystalline solids. However, the phonon gas model struggles to accurately describe thermal conductivity in materials whose mean free path length approaches the interatomic distances, e.g., glasses[26], materials with pronounced anharmonicity[22,27], a sufficient degree of atomic disorder[28] or large unit cells[29]. In such materials, heat is conducted via a fundamentally different type of phonons, denoted as “diffusons”. Instead of propagating through the crystal, their conduction mechanism can rather be thought of as a random-walk of thermal energy.[29] Small interband spacing found in materials with a large unit cell, and high phonon linewidths, evoked by anharmonic interactions, facilitate the overlap of phonon modes and promote diffuson-type thermal transport. As phonon linewidths increase with temperature, diffuson-type thermal transport increases with temperature too and saturates at high temperature.[22] Both types of thermal transport are not exclusive but can contribute in parallel to a materials thermal conductivity. Different two-channel theories and models have been developed to separate the total thermal conductivity by the respective channels.[28–30] The distinction into phonon gas and diffuson channel is heavily based on the characteristics of the underlying lattice vibrations. It is yet unclear how the previously observed change from Debye-like to liquid-like phonon dynamics observed in lithium argyrodites transfers to the thermal conductivity and which role local disorder, strongly prevalent in lithium-argyrodites[9], and disrupted long-range structural correlation play.

To investigate these influences, utilizing various characterization techniques is required. Via X-ray diffraction experiments reduced particle size and the introduction of microstrain upon enhanced mechanical energy input in two exemplary argyrodites, $Li_{5.5}PS_{4.5}Cl_{1.5}$ and Li_6PS_5Br, is revealed. The pair-distribution function (PDF) extracted from total scattering experiments additionally yields information about the short- and long-range local structure. Corresponding refinements quantify the decrease in coherence length and indicate increased local disorder. To probe interrelations of local structure and loss of coherence, including diminished crystallite size, introduced strain, and structural disorder, with the diffusion coefficient, quasi-elastic neutron scattering (QENS) is performed, whose activation energies are compared with electrochemical impedance spectroscopy (EIS) results. These experiments demonstrate that the reduction in coherence length strongly affects the ionic conductivity of $Li_{5.5}PS_{4.5}Cl_{1.5}$ and Li_6PS_5Br, highlighting the importance of tailored processing procedures for electrolytes to maximize their ionic transport in fabricated solid-state batteries.

The post-synthesis treatment may not only influence structure and ionic transport but also vibrations within the lattice. Via Raman spectroscopy as well as inelastic neutron scattering (INS), changes in the atomic frequencies and phonon density of states (DOS) are probed. Those experiments are validated by ab-initio lattice dynamics calculations, which provide additional insights into the local frequency distribution. Based on these characterizations, differences in the temperature dependence of the thermal transport are evaluated. Contrary to the ionic conductivity, thermal transport and vibrational properties are affected only to a minor degree by loss of coherence. To further deconvolute the effects of structural disorder and loss of coherence, the $Li_6PS_5Br_xI_{1-x}$ substitution series is additionally investigated, to discern the influence of disorder within the series. This structural disorder is found to heavily influence thermal conductivity, especially at low temperatures.

This work offers a localized view of lithium-ion vibrations in these materials, uncovering the anharmonic character that gives rise to the recently observed liquid-like dynamics. These dynamics, in turn, lead to intrinsically low lattice thermal conductivities, providing deeper insight into the fundamental nature of fast ionic conductors.

Experimental section

Lattice dynamics. The required ordering of the unit cell for density functional theory (DFT) calculations requires distributing 24 Li^+ ions across 120 positions (T2, T5, and T5a), resulting in ≈10^{25} possible permutations, not considering the anion site disorder. To simplify this, the primitive unit cell, containing one formula unit, was used.[31] As the number of ions on each site in the primitive cell must be an integer, the occupancies were adopted accordingly. Given that the primitive unit cell contains only one halide atom, only 0% or 100% anion disorder scenarios to be calculated. Here, 0% disorder was chosen, as it is closer to the experimentally found disorder. Additionally, $Li_{5.5}PS_{4.5}Cl_{1.5}$ could not be calculated due to the non-integer numbers of Li, S, and Cl atoms. Li_6PS_5Cl was calculated instead. Considering the similarities of lattice dynamical properties of Li_6PS_5Br and Li_6PS_5Cl, properties of $Li_{5.5}PS_{4.5}Cl_{1.5}$ can be approximated by Li_6PS_5Cl with high accuracy. Crystal structures of Li_6PS_5Br and Li_6PS_5Cl were taken from literature.[9] All structural orderings were cleaned of symmetrically equivalent duplicates and the remaining structures relaxed employing DFT. All DFT were performed using the Vienna Ab Initio Simulation Package (VASP)[32–34] and utilizing projected-augmented-wave (PAW) potentials[35]. The exchange correlation energy was calculated using the PBEsol functional within the generalized gradient approximation (GGA).[36] The PAW potentials used were Li_sv 10 Sep 2004 $1s^2 2s^1$, P 06 Sep 2000 $3s^2 3p^3$, S 06 Sep 2000 $3s^2 3p^4$, Cl 06 Sep 2000 $3s^2 3p^5$, and Br 06 Sep 2000 $4s^2 4p^5$. During relaxation the atomic positions and unit cell volume were allowed to relaxed. Detail on computational parameters can be found in Table S1. The structure with the lowest energy was taken for further lattice dynamics calculations. The resulting lattice parameters and a comparison to experimentally found lattice parameters is given in Table S2. Finally, the phonopy package[37,38] was utilized for generating the displacements and post-processing. Computational details on the force calculations are given in Table S3.

Synthesis. Syntheses of $Li_6PS_5Br_xI_{1-x}$ ($x = 0$, 0.1, 0.2, 1), and $Li_{5.5}PS_{4.5}Cl_{1.5}$ were performed under argon atmosphere. The stoichiometric amounts of Li_2S (thermo scientific, 99.9%), P_4S_{10} (Sigma-Aldrich), LiCl (Alfa Aesar, 99%), LiBr (Alfa Aesar, ≥99%), and LiI (thermo scientific, 99.999%) were ground in an agate mortar for 15 min, pelletized, and sealed under vacuum in carbon-coated quartz ampoules. The ampoules were dried at 800 °C for 2 h under dynamic vacuum prior to use to remove any traces of humidity. All syntheses were conducted in tube furnaces set to a heating rate of 100 °C · h^{-1} and natural cooling after the reaction. $Li_{5.5}PS_{4.5}Cl_{1.5}$ was synthesized by heating the precursors to 450 °C for 3 days twice. In between both runs the sample was ground, pelletized, and sealed as described above. $Li_6PS_5Br_xI_{1-x}$ was made by heating the precursors to 550 °C for 2 weeks. After the syntheses the products were hand-ground before further processing and characterization.

Samples of four different coherence length synthesized by different post-synthesis treatment procedures.[18] The first sample, referred to as pristine or simply XL (extra-long coherence length), received no further treatment. The second part with long coherence length (L) was shaken for 10 min at 40 Hz utilizing a Fritsch PULVERISETTE 23. 200 mg of pristine argyrodite and five 5 mm ZrO_2 balls were put in a 15 mL ZrO_2 cup. The third and fourth processing method included a Fritsch PULVERISETTE 7 premium line planetary ball mill. 1 g of pristine argyrodite was mixed with 10 g milling media (5 mm ZrO_2 balls) in an 80 mL ZrO_2 cup. Each milling cycle consisted of 10 min milling time at 500 rpm and 10 min resting time. For one sample only a single cycle was performed, the other one was milled for 24 cycles (4 h total milling time). The resulting samples with medium and short coherence length are consequently referred to by M and S, respectively.

The samples for quasi- and inelastic neutron scattering experiments were made using ^{7}Li enriched precursors ($^7Li_2S$, ^{7}LiCl, and ^{7}LiBr, Sigma Aldrich, ≥99 atom % ^{7}Li, ≥99% purity). The masses were adopted to account for the altered molar masses. The synthesis and post-synthesis procedures remained the same. However, due to limited beam time and the cost of the precursors only the pristine and 4 h milled (XL and S) samples were investigated.

Electrochemical impedance spectroscopy. Ionic conductivities were determined using potentiostatic electrochemical impedance spectroscopy. Pellets of 300 mg to 400 mg were pressed isostatically at 500 MPa for 40 min, resulting in relative densities of 83% to 88% (see Table S6). On either side of these pellets 100 nm thick gold electrodes were sputtered. The pellets were sealed in pouch cells and the electrodes contacted using Al current collectors. Impedance spectra were acquired in a temperature range from −120 °C to 60°C and a frequency range for 25 mHz to 10 MHz employing an Alpha-A impedance analyzer (Novocontrol Technologies) with a root-mean-square excitation voltage of 20 mV. To ensure thermal equilibration each temperature was held for 1 h before starting the impedance measurements. The impedance spectra were fitted using the RelaxIS 3 software by rhd instruments. Where possible, the impedance response was fitted with a constant phase element (CPE) for the blocking behavior of the gold electrodes and a (R)(CPE) element for the bulk grain boundary contributions. For measurements with insufficient data points to fit the (R)(CPE) element, this element was replaced by an ohmic resistor.

X-ray scattering. X-ray diffractograms were collected on a Stoe STADI P diffractometer in Debye-Scherrer geometry equipped with a Ge(111) monochromator and a Dectris MYTHEN2 1K detector. Samples were sealed in glass capillaries with a diameter of 0.5 mm. For the Williamson-Hall analyses and analyses of the amorphous content Cu $K_{\alpha1}$ radiation ($\lambda = 1.540562$ Å) was used. The diffractograms were measured in a 2θ range from 10° to 90° with a step size of 0.015°. Williamson-Hall analysis was used to quantify the strain ε of the materials according to Equation (1).[39]

$$\beta \cos\theta = 4\epsilon \sin\theta + \frac{K\lambda}{L} \tag{1}$$

The peak broadening was quantified by the integral breadth β of each individual reflection of X-ray diffraction data. A pseudo-Voigt function was used to fit the intensity of each individual Bragg reflection as described elsewhere[40]. The constant K was assumed to be 0.9, corresponding to spherical crystallites, while strain ε and crystallite size L were then extracted by linear regression in a Williamson-Hall plot. For the analyses of the amorphous content the argyrodite sample was mixed with silicon powder (20 wt%). Comparison of actual and Rietveld refined percentage by weight of argyrodite yields the argyrodite's amorphous fraction (Tables S3 and S4).

Low temperature X-ray diffractograms were measured in a 2θ range from 6° to 40° with a step size of 0.015° using Mo $K_{\alpha1}$ radiation ($\lambda = 0.70932$ Å). The sample temperature was controlled by employing a Cryostream 1000 (Oxford Cryosystems). For each sample short measurements were conducted in 4 K intervals, with prolonged measurements at specific temperatures.

For pair distribution function analyses (PDF) total scattering data was measured on a Stoe STADI P diffractometer in Debye-Scherrer geometry using Ag $K_{\alpha1}$ radiation ($\lambda = 0.5594075$ Å), a Ge(111) monochromator and four Dectris MYTHEN2 1K detectors.[41] Samples were sealed in glass capillaries with a diameter of 0.5 mm and measured over a Q-range of 0.8–20.5 Å^{-1}. Data reduction was done using PDFgetX3[42] with a Q-range cutoff of $Q_{\max} = 15$ Å^{-1}. Small box modeling of PDF done using TOPAS academics V7.[43] The data were fitted in a r-range of 1.8 Å to up to 120 Å. For each sample the r-range was first limited to 10 Å and successively increased in 10 Å steps to 120 Å. The final model of an iteration was used as input for the subsequent $r_{\max}$ value. For each model the (1) scale factor, (2) correlated motion factor, (3) spherical diameter, (4) lattice parameters, (5) atomic positions, (6) isotropic atomic displacement parameters, and, in case of Li_6PS_5Br, (7) the occupancies were refined.

Quasi-elastic neutron scattering (QENS). QENS measurements were performed using the BASIS backscattering spectrometer[44] at the Spallation Neutron Source (SNS) at the Oak Ridge National Laboratory (ORNL). Due to limitations of beam time, only samples with the highest and lowest coherence length were investigated, i.e., pristine and 4 h ball-milled samples. 5 g of ^{7}Li enriched (>99% ^{7}Li) argyrodite samples were filled under inert conditions into aluminum sample holders (1 mm-spaced double wall cylinder), sealed with aluminum foil as a gasket and loaded in a closed-cycle refrigerator with a hot stage. The pristine samples were measured at 60 K, 300 K, 350 K, 400 K, 500 K, and 600 K, whereas the ball-milled samples were measured at 250 K (only $^7Li_6PS_5Br$), 300 K, 325 K, and 350 K to avoid recrystallization of the samples. Additionally, brief measurements every 10 K were performed upon heating from 60 K to the maximum temperature. At 60 K, diffusion was assumed to occur on timescales slower than those accessible by BASIS. Consequently, data measured at this temperature were taken as sample-specific instrument resolution function. Si(111) analyzers were used with a neutron wavelength centered around 6.4 Å and a chopper frequency of 60 Hz. This configuration allows to access a Q-range of 0.2–2 Å^{-1} with energy transfers of −120 μeV to 120 μeV. The data was reduced, normalized against a vanadium standard, and grouped into Q bins of 0.2 Å^{-1} width and energy bins of 0.8 μeV width using the Mantid software package[45]. The $S(Q,E)$ was fitted using a delta function $\delta(E)$ and a Lorentzian with the half width at half maximum $\Gamma(Q)$, representing the elastic signal and the quasi-elastic broadening, respectively. Both functions were centered around energy E_0, convoluted with the resolution function $R(Q,E)$, and scaled using the parameters A and B. Additionally, a linear background $C(Q,E)$ was considered. Fitting of $S(Q,E)$ was performed using the Dave software package[46].

$$S(Q,E) = \left(A\delta(E-E_0) + B\frac{\pi\Gamma(Q)}{\Gamma(Q)^2 + (E-E_0)^2}\right) * R(Q,E) + C(Q,E) \qquad (2)$$

Data of the pristine samples was analyzed using the Chudley-Elliott model[47], capable to obtain jump distances d, mean residence times τ, and thereby diffusion coefficient.

$$\Gamma(Q) = \frac{\hbar}{\tau}\left(1 - \frac{\sin(Qd)}{Qd}\right) \tag{3}$$

According to random walk theory, the diffusion coefficient is given by

$$D = \frac{d^2}{6\tau}. \tag{4}$$

Inelastic neutron scattering (INS). Inelastic neutron scattering experiments were performed at the ARCS neutron time-of-flight spectrometer[48] at SNS, ORNL using the exact same ^{7}Li-enriched samples as in the QENS experiments, i.e., with the highest and lowest coherence length. Samples were loaded into ½ inch cylindrical aluminum cans. To eliminate peak broadening due to ionic diffusion all measurements were conducted at a sample temperature of 100 K. Scattering data were recorded for incident neutron energies of E_i = 15 meV, 40 meV, and 100 meV, a slit spacing of 1.5 mm, and chopper speeds of 240 Hz, 360 Hz, and 600 Hz, respectively. $Li_{5.5}PS_{4.5}Cl_{1.5}$ was additionally measured at an incident neutron energy of 200 meV. At each energy the background of an empty aluminum can was collected and subtracted from the sample data after data reduction. Slight variations in detector efficiency were removed by normalization to a white beam V data set. For data reduction the Mantid DGS package was used.[45] A measurement on a vanadium standard was used to correct the data for detector efficiency. The analysis of the phonon DOS was performed within the incoherent scattering approximation and corrected for the effect of multiphonon scattering in an iterative procedure using the multiphonon package.[49] The neutron weighted simulated density of states (DOS) $g_{\mathrm{sim}}(E)$ was calculated using the atom-projected calculated phonon DOS $g_j(E)$ of each element and weighing it with respect to its total neutron scattering cross-section σ_{tot} and the atomic mass m_j.

$$g_{\mathrm{sim}}(E) = \frac{\sum_j \frac{\sigma_{\mathrm{tot}}}{m_j} g_j(E)}{\sum_j \frac{\sigma_{\mathrm{tot}}}{m_j}} \tag{5}$$

As no calculated phonon DOS for $Li_{5.5}PS_{4.5}Cl_{1.5}$ was available, the phonon DOS of Li_6PS_5Cl was used and adopted for the different atomic composition in $Li_{5.5}PS_{4.5}Cl_{1.5}$.

Neutron powder diffraction. Samples of Li_6PS_5Cl, Li_6PS_5Br, and $Li_{5.5}PS_{4.5}Cl_{1.5}$ were measured on the high-resolution powder diffractometer D2B at the Institut Laue-

Langevin using neutrons with a wavelength of 1.594 Å and a 2Θ range of 11 ° to 160 °. 3 g of sample were loaded under argon atmosphere into 8 mm diameter vanadium cans which were sealed with indium wire. Samples below room temperature were cooled using a top-loaded cryostat. Neutron powder diffraction on Li_6PS_5I was performed at the POWGEN beamline[50] at SNS, ORNL. 2.5 g of Li_6PS_5I were loaded into a 6 mm vanadium can, sealed with a Cu gasket. Neutrons with wavelengths centered around 0.8 Å were used for data collection. Sample environment was controlled using the POWGEN Automatic Changer.

Rietveld refinements. Rietveld refinements against X-ray and neutron diffraction data were performed with the TOPAS Academic V7 software package.[43] Refinements included (1) a scale factor, (2) background using a Chebyshev polynomial function, (3) a zero offset, (4) instrumental parameters, (5) peak shape parameters from the modified Thompson-Cox-Hastings pseudo-Voigt function[51], (6) lattice parameters, (7) site fractional coordinates, (8) occupancy factors, and (9) isotropic displacement parameters. Finally, all parameters were refined simultaneously to ensure stability of the parameters and a converged refinement. The quality of the refinements was assessed using the R_{wp} and the goodness-of-fit (GoF) values as indicators.

Raman spectroscopy. Raman spectra were acquired using a SENTERRA II spectrometer by Bruker, equipped with a 532 nm laser. In-house made sample holders were used to protect the samples against ambient moisture. Each spectrum was measured with a laser power of 2.5 mW, an integration time of 5 s and 5 coadditions in a range of 50–1425 cm^{-1} with a resolution of 1.5 cm^{-1}.

Thermal conductivity. Thermal conductivities were measured with the Thermal Transport Option of a Physical Property Measurement System (PPMS) DynaCool (Quantum Design). Due to the low thermal conductivity samples were measured in two-probe lead configuration using disk shaped samples. Samples were first consolidated with a vice press using a 4 mm pressing tool and subsequently pressed isostatically at 500 MPa for 40 min. Flash sintered pellets were sealed in carbon-coated quartz ampoules (see Section Synthesis) inserted into a tube furnace preheated to the synthesis temperature, annealed for 15 min and the cooled naturally inside the furnace. Sample leads were attached using EPO-TEK® H20E two-component epoxy glue and a curing procedure of 80 °C for 3 h. Thermal conductivities were measured in a temperature range of 2 K to 300 K with a temperature rise of 3%.

High-temperature thermal conductivities of Li_6PS_5I were determined using a LFA 467 HyperFlash® setup by Netzsch. Below room temperature a MCT detector with a ZnS furnace window was used, whereas above room temperature an InSb detector with a sapphire furnace window was employed. Measurements were performed in inert atmosphere of pure nitrogen with a flow of 100 sccm. The sample was spray-coated with a graphite layer to enhance absorption and emission of infrared light. Detection time and signal amplification were optimized automatically during the measurement. Three measurements were performed at each temperature (five measurements at 173 K) and the detector signal is fitted with an improved Cape-Lehman model.[52,53] The obtained thermal diffusivity α can be converted to thermal conductivity κ using isobaric heat capacity c_p and density ρ.

$$\kappa = \alpha \cdot c_p \cdot \rho \tag{6}$$

The isobaric heat capacity was approximated by the isochoric heat capacity obtained from density functional theory-based lattice dynamics calculation. The density was determined geometrically.

Results & Discussion

Li_6PS_5Br and $Li_{5.5}PS_{4.5}Cl_{1.5}$ represent two of the most widely studied argyrodite-type solid electrolytes in the field of lithium solid-state batteries. While their fundamental properties have been extensively characterized in the as-synthesized, pristine state, the influence of post-synthetic processing, e.g., for cathode composite fabrication, remains insufficiently understood. In this study, four samples of each argyrodite are subjected to varying degrees of mechanical energy input after the synthesis, to systematically investigate the influence of structural coherence on the ionic and thermal transport. Where required, comparative data for both compounds are provided. In cases where only one dataset is displayed in the main text, results for Li_6PS_5Br are shown, with the corresponding data for $Li_{5.5}PS_{4.5}Cl_{1.5}$ available in the Supporting Information.

Loss in coherence

To correlate changes in the materials dynamics with the coherence length, first structural details in Li_6PS_5Br and $Li_{5.5}PS_{4.5}Cl_{1.5}$ are analyzed by total scattering and Williamson-Hall analyses. The influence of post-synthesis processing on both the average and local structure, as well as on the coherence length, can be analyzed via the reduced pair distribution function $G(r)$. All $G(r)$ exhibit a decay of intensity (structural coherence) at increasing interatomic distances r. As previously reported by Maus et al.[18], this decay is intensified with enhanced energy input of the post-synthesis processing (Figure 2b and S1a, refinements in Figures S3 and S5). In the following the labels “XL”, “L”, “M” and “S” are used, corresponding to the respective coherence length (extra-long, long, medium and short) of each processing method (Figure 2a). The reduction in coherence is corroborated by Williamson-Hall analyses (Figure 2d and S1c), which enable the deconvolution of crystallite size and strain contributions induced during processing, rather than providing only a total coherence length. While negligible strain is observed in the XL samples, increasing the energy input employing different post-synthesis processing methods and thereby reducing coherence length, introduces more and more strain. At the same time, enhanced energy input also leads to a reduced crystallite size, confirming the trend of diminished coherence lengths (Figure 2e and S1d). Specific energy inputs were taken from previous simulations.[18] Owing to the minimal peak broadening in the Bragg reflections used for the

Williamson–Hall analyses and the gradual coherence decay observed in the *G*(*r*), both techniques face limitations in reliably quantifying large crystallite sizes and coherence lengths for the more crystalline compounds, respectively, resulting in noticeable uncertainties for high values.

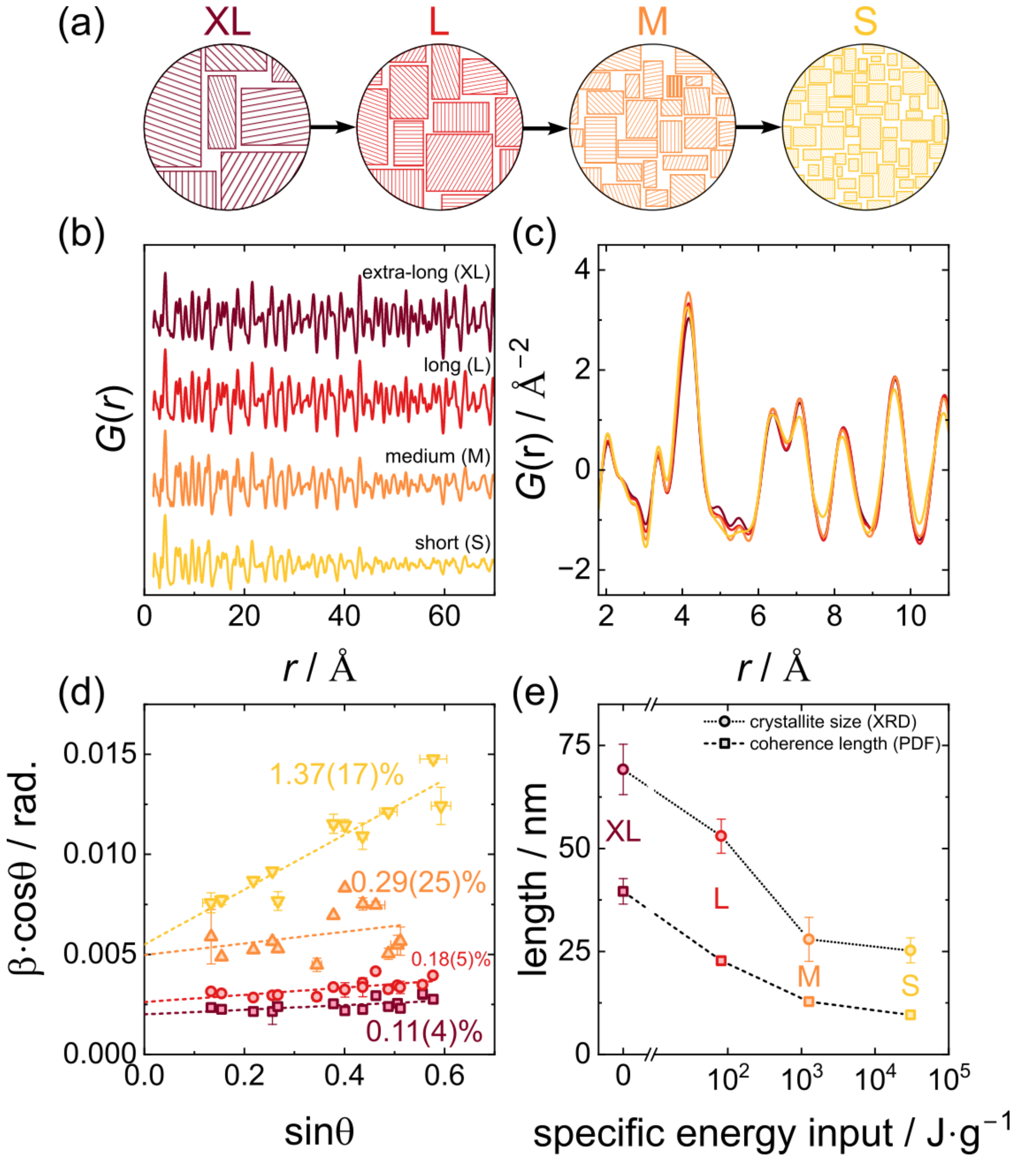

Figure 2. (a) Schematic reduction of crystallite size and coherence length across the differently labeled samples. (b) Long- and (c) short-range G(r) of Li_6PS_5Br for the different post-synthesis processing methods indicating the amount of local disorder and the loss in coherence. The peaks at the lowest distances of 2.1 Å and 3.4 Å can be assigned to P-S and S-S bonds of the PS_4^{3-} unit, respectively. (d) Williamson-Hall analysis of Li_6PS_5Br samples with increasing amounts of strain and lower crystallite size, indicated by the higher y-axis intersect for samples with lower coherence lengths. The XRD patterns depicting the peak broadening are given in Figure S7. (e) Coherence length as obtained from fits of G(r) and crystallite size from the Williamson-Hall analysis as a function of energy input. Although

both methods differ of up to a factor of 2, the general trend and order of magnitude agree for both methods. An analogous plot for $Li_{5.5}PS_{4.5}Cl_{1.5}$ *is given in Figure S1.*

Less significant differences of the *G*(*r*) between the different processing methods are observed at low distances (Figure 2b and S1b) demonstrating that the processing does not affect the local structure of the materials. In both argyrodites, almost no differences can be seen at the shortest bonds present in the materials: the P-S bond within the PS_4^{3-} tetrahedra and the Li^+-X^-/S^{2-} distances. Due to the small scattering cross section of lithium, the latter is only visible as small peak in $Li_{5.5}PS_{4.5}Cl_{1.5}$ and shoulder in Li_6PS_5Br. Thus, even for short coherence length the first coordination sphere in the argyrodite is preserved. Despite the well-known structure of lithium argyrodites, refining the short-range *G*(*r*) (Figures S2 and S4) poses significant difficulties, e.g., the observed peak around 3.4 Å cannot be fitted by the standard cubic model. It has been suggested that a tilting of the PS_4^{3-}, resulting in a symmetry reduction, could fit this distance.[54,55] At larger distances however, the lowest-coherence sample in Li_6PS_5Br and the two samples with lowest coherence in $Li_{5.5}PS_{4.5}Cl_{1.5}$ exhibit broader peaks with reduced intensity compared to the pristine counterpart (Figure S6). Consequently, the fitting of these data required higher atomic displacement parameters, which is indicative of increased disorder in the local structure. Despite this disorder, diffraction experiments with silicon as internal standard revealed that in all samples almost no amorphous content is present (Tables S4 and S5). So, while the post-synthesis procedures lead to a loss of coherence, reduced crystallite size, strain, and local disorder, they do not amorphize the solid electrolyte.

Li^+ ion dynamics and diffusion

The ionic conductivity of solid electrolytes is a critical parameter governing the performance of solid-state batteries and is influenced by multiple structural and microstructural factors, including coherence length and local structure.[18] To assess the impact of the different post-synthesis processing procedures on the ionic conductivity of Li_6PS_5Br and $Li_{5.5}PS_{4.5}Cl_{1.5}$ electrochemical impedance spectroscopy (EIS) was performed. Spectra of all samples throughout the entire temperature range were well resolved and could be fitted with either a (R-CPE)-CPE or R-CPE equivalent circuit. Fits of data measured at 173 K and 298 K are given in Figures S9 to S12. α-values of the CPEs of close to unity are indicative of almost ideally capacitive behavior, i.e., perfect blocking behavior of the electrodes and uniform relaxation times. Across all samples, the Nyquist plots displayed a single, well-defined semicircle, preventing the deconvolution of bulk and grain boundary contributions. Therefore, all values reported correspond to total ionic conductivities.

In both argyrodites, the room-temperature ionic conductivity changes non-monotonically with respect to the coherence length. For both materials, moderate reductions in coherence length, associated with milder processing, lead to a slight increase in ionic conductivity (Figure 3a). However, with further reduction in coherence length, resulting from harsher treatments, the conductivity decreases. The observed maximum in ionic conductivity might be caused by two opposing effects. First, previous studies have shown that smaller particle sizes result in better transport properties in cathode composites.[16,56] Although particle size and crystallite size are not the same and in principle independent of each other the processing procedures not only decrease crystallite size but also particle size[18], which consequently results in an increased ionic conductivity. Second, the increase in local disorder at small *r* observed for low coherence lengths, especially in $Li_{5.5}PS_{4.5}Cl_{1.5}$ is believed to impede ionic transport as it alters inter-cage distances important for long-range ionic transport and thereby disrupts the interconnected 3D network of lithium-ion conduction pathways.[9,10] In combination, these two opposite effects can result in the observed increase in ionic conductivity due a reduction in particle size for mild processing, while for higher energy input the reduction in crystallite size dominates, reducing ionic conductivity. Notably, in the chloride-rich argyrodite, the conductivity maximum is reached at comparatively higher coherence lengths, and the subsequent decline in conductivity is more pronounced than in the bromine analogue. This drop in ionic conductivity for low coherence lengths is consistent with previous reports for $Li_{5.5}PS_{4.5}Cl_{1.5}$.[18] The less severe reduction of ionic conductivity for the bromide argyrodite could be linked to the strain introduced, which has been shown to enhance ionic conductivity in this system.[40] Throughout the series of processing conditions, the activation energy that remains is only minimally affected with changes of less than 0.03 eV ($Li_{5.5}PS_{4.5}Cl_{1.5}$ up to ≈−6%, Li_6PS_5Br up to ≈−4.5%) (Figure 3b). As no deconvolution of bulk and grain boundary contributions is possible (see Figures S9 and S12), it remains elusive if the changes in ionic conductivity are caused by a changing prefactor of bulk transport, by a change in grain-boundary resistances or both. However, based on the unchanged first coordination sphere (Figure 2c), virtually identical frequencies as observed with Raman spectroscopy (Figure S13), and similar phonon densities of states (Figure 4a and b), jump distance, attempt frequency, and migration entropy are not expected to change strongly, keeping the prefactor of bulk transport relatively constant. Thus, the grain-boundary resistance is assumed to be the main contributor to a change in ionic conductivity.

To gain further insights into the (change of) diffusion mechanism and ion dynamics in the argyrodites, quasi-elastic neutron scattering (QENS) experiments were conducted for comparison on the XL and S samples, corresponding to samples with the highest and lowest coherence length, respectively. X-ray diffraction analyses carried out on the low-coherence sample after sequential heating revealed the onset of recrystallization at approximately 373 K.[18] Consequently, the QENS measurements on those samples were restricted to temperatures below this threshold, with a maximum of 350 K. By interacting with diffusing lithium ions, neutrons can gain or lose energy, resulting in a broadening of the elastic signal. This broadening, indicative of ionic motion, becomes apparent above 250–300 K, manifesting as an onset in quasi-elastic intensity (Figure S14a and b).[57] With increasing temperature, this broadening becomes significantly more pronounced as diffusion becomes faster and more ions become mobile. By integrating the quasi-elastic and background scattering intensity at different temperatures and normalizing to the lowest temperature (here 60 K), the onset of diffusion can be identified. As higher quasi-elastic intensity corresponds to an enhanced fraction of mobile ions, a qualitative comparison of the temperature-dependent fraction of mobile ions within the material can be performed (Figure S14a and b). The onset of diffusion in XL Li_6PS_5Br occurs approximately 30 K earlier than in XL $Li_{5.5}PS_{4.5}Cl_{1.5}$. Although the room-temperature conductivity of $Li_{5.5}PS_{4.5}Cl_{1.5}$ is higher than that of Li_6PS_5Br, the lower activation energy of the bromine argyrodite, allows for higher conductivity at low temperatures, which is confirmed by the earlier onset of quasi-elastic intensity. For both materials, lower relative intensities above 300 K are observed for the samples with low coherence length compared to highly coherent samples. However, given the short measurement time at each temperature step, these differences are possibly within the experimental uncertainties.

The unprocessed, pristine samples can be heated to significantly higher temperatures than the low coherence samples, giving rise to a more intense (Figure S14a and b) and broader (Figure S14c) quasi-elastic signal, which can be fitted by a Lorentzian function. An exemplary fit of the entire signal according to Equation (2) is given in

Figure S14d. The *Q*-dependence of the linewidth of this Lorentzian allows a more detailed analysis using the Chudley-Elliott model.[47] Although in general this model allows to obtain the jump distance of the ions, the extraction of the jump distance is less reliable and more error-prone than the fit of the relaxation time. So, previously reported crystallographic inter-cage jump distances of 2.8 Å[11] and 3.1 Å[9] for $Li_{5.5}PS_{4.5}Cl_{1.5}$ and Li_6PS_5Br, respectively, were used to guide the fit (Figure 3c and Figure S15). A previous study investigating the ion dynamics of closely related Li_6PS_5Cl confirmed, that the QENS signal is dominated by the inter-cage dynamics.[14] Fits in which the jump distance was refined too, yield jump distances comparable to crystallographic jump distances (Figure S16, Tables S7 and S8). Using the fitted mean residence times and the crystallographic jump distances, the Li^+ diffusion coefficients were calculated by employing Equation (4). The obtained diffusion coefficients follow closely an Arrhenius-type behavior with activation energies of 0.176(6) eV for $Li_{5.5}PS_{4.5}Cl_{1.5}$ and 0.0925(4) eV for Li_6PS_5Br (Figure 3d). At the lowest temperatures, the linewidth is almost independent of *Q*, which could indicate localized diffusion between two lattice sites. This can be expected as the intra-cage doublet jump between two T5 sites is associated with a lower activation energy than the inter-cage T2-T2 jumps and thus particularly favored at low energies.

Since QENS probes dynamics on shorter length scales than impedance spectroscopy, the activation energies derived from QENS are significantly lower than those from impedance measurements (typically 0.3 eV to 0.4 eV) (Figure 3b). Additionally, QENS selectively captures local ion hopping processes and is thus insensitive to microstructural features such as grain boundaries, which can alter the apparent activation behavior. Despite these methodological differences, the relative trend is consistent: a higher activation energy is found for $Li_{5.5}PS_{4.5}Cl_{1.5}$ compared to Li_6PS_5Br. Given the multitude of nuclear magnetic resonance (NMR) methods and their vastly different timescales and methodologies, comparing the activation energy and diffusion coefficients requires careful consideration.[58] Nevertheless, activation energies obtained from QENS match those obtained by NMR methods probing short timescales and fast dynamics (see Tables S9 and S10 for detailed comparison) and are consistent with the previously reported 0.11 eV for Li_6PS_5Cl extracted from QENS data[14].

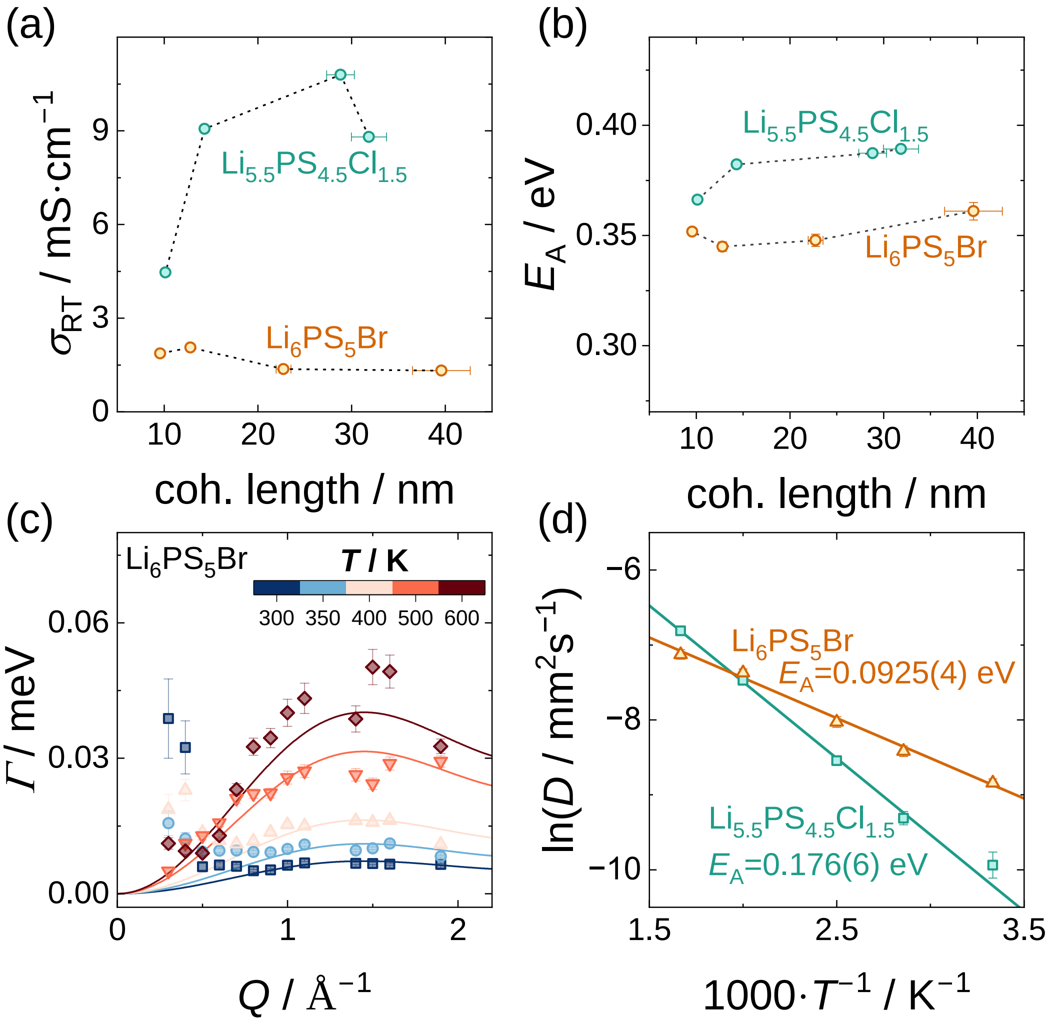

Figure 3. (a) Room-temperature ionic conductivities measured with impedance spectroscopy with respect to the coherence length. (b) Activation energies derived from temperature-dependent impedance spectroscopy. (c) Q-dependence of the Lorentzian linewidth at various temperatures for Li_6PS_5Br and corresponding fits using the Chudley-Elliott model. Q bins with considerable contributions by Bragg peaks were excluded and are not shown in this plot. The corresponding plots for $Li_{5.5}PS_{4.5}Cl_{1.5}$ can be found in Figure S15. (d) Arrhenius plot of the diffusion coefficients obtained from the fits with the Chudley-Elliott model. Both argyrodites exhibit an Arrhenius-type behavior with higher activation energy found for $Li_{5.5}PS_{4.5}Cl_{1.5}$.

Lattice dynamics on global and local scale

The fast ion dynamics of lithium ions culminates in a breakdown of phonon modes at high temperatures, preventing classic solid-state lattice dynamics to accurately capture phonons in these systems.[14] At low temperatures, however, lattice dynamics on a local scale can provide insights into ion dynamics and transport beyond structural arguments and results inferred from measurements of diffusion or conductivity via EIS, QENS or NMR. Previous work has employed different lattice dynamics-based approaches to track changing lattice dynamics within substitution series allowing to better understand ionic transport[59], demonstrated that vibrations in the direction of ionic transport possess extraordinarily low frequencies[22], or elucidated the role of different degrees of freedom on ionic transport[23,60]. Therefore, here the lattice dynamics of Li_6PS_5Br and $Li_{5.5}PS_{4.5}Cl_{1.5}$ are characterized by both experimental and computational methods. Experimentally derived phonon densities of states (phonon DOS) from inelastic neutron scattering reflect the total DOS and cannot be decomposed into atom-, site-, or direction-specific contributions, but may capture the microstructural effects. Vice versa, density functional theory (DFT) calculations performed under periodic boundary conditions model idealized single crystals and thus exclude microstructural influences. While this limits direct comparability to real samples in terms of coherence length and disorder, calculated phonon DOS enable decomposition of the vibrational spectra by atomic species, crystallographic site, and even spatial direction, offering detailed, local insights into vibrational modes relevant to ionic transport. For a holistic study of vibrations in argyrodites on a global and local scale, inelastic neutron scattering experiments with lattice dynamics calculations are combined here.

Despite the differences observed in X-ray diffraction measurements and the reduced coherence length, the phonon DOS of XL and S samples are similar, both for the bromine (Figure 4a, S17a, S18a) and the chloride (Figure 4b, S17b, S18b) argyrodite, and independent of the incident neutron energy (15 meV for Figure S17, 40 meV for Figure 4a, and 100 meV for Figure S18). This outcome aligns with prior studies[61,62] showing similar phonon DOS in fully amorphous and fully crystalline forms of the same material. Given the high scattering cross-section of Cl^- ions and the confined frequency range of the corresponding vibrations, the neutron-weighted DOS (NWDOS) of $Li_{5.5}PS_{4.5}Cl_{1.5}$ exhibits a peak at low frequencies, which was also observed in the experimental phonon DOS. Nevertheless, the experimentally measured DOS of both argyrodites contain a peak at 14 THz (Figure S18), which is not predicted by the calculated NWDOS, but was previously also found in Li_6PS_5Cl and linked to vibrations of PS_4^{3-} tetrahedra.[14]

Raman spectroscopy offers, compared to the INS-measured phonon DOS a much higher frequency resolution, enabling to detect small frequency changes. This high resolution enabled to detect a slight red-shift of approximately 0.04 THz for the ball-milled samples (Figure S13a), corresponding to an almost unnoticeable softening of the lattice. Although this shift is close to the resolution of the instrument (0.045 THz) fits of the peak shape confirmed this shift. As the high frequency vibrations of the PS_4^{3-} units (at 17 THz to 18 THz, corresponding to approx. 570 cm^{-1} to 600 cm^{-1}) are Raman-active, they can be used to check the accuracy of the atom-projected DOS of phosphorous, revealing good agreement between measured and calculated frequencies (Figure S13b).

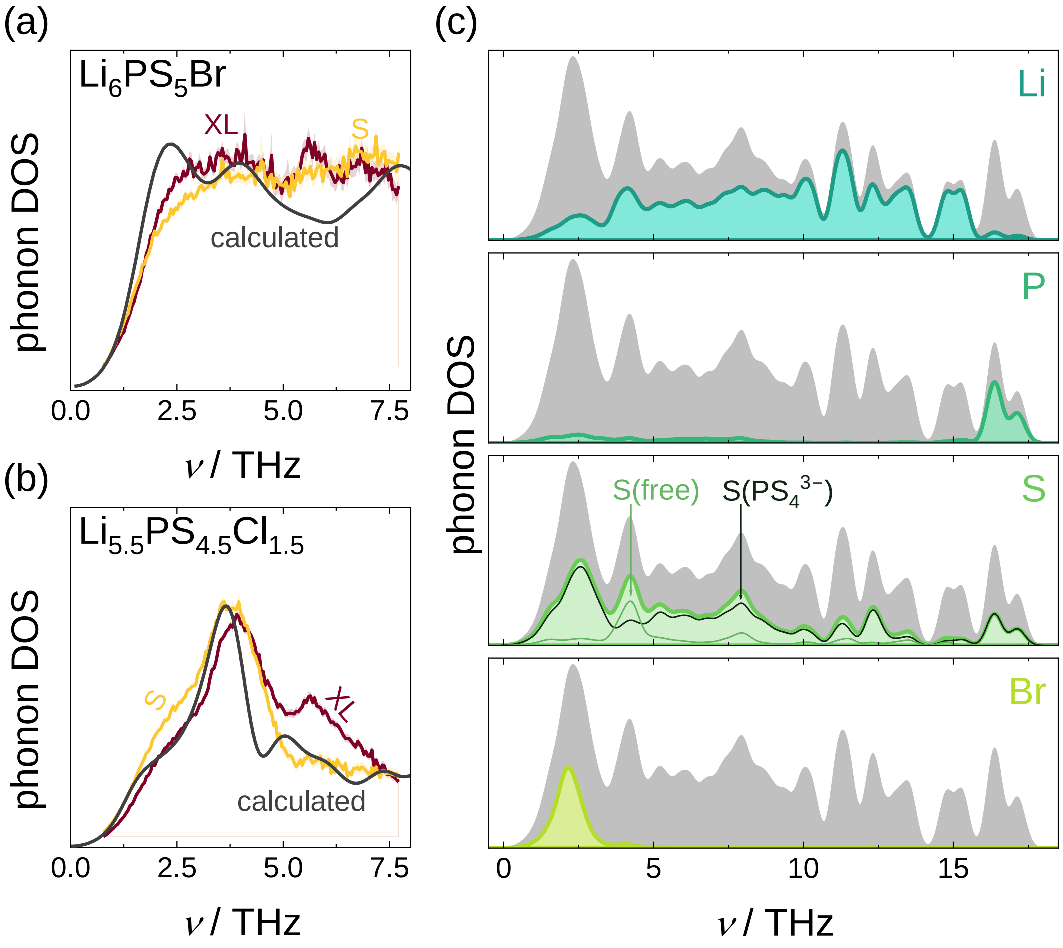

Figure 4. (a) and (b) Phonon DOS at 100 K as obtained from inelastic neutron scattering experiments using neutrons with 40 meV incident neutron energy as well as the modelled neutron-weighted phonon DOS. "XL" and "S" denote the coherence length of the respective sample. (c) Calculated atom-projected phonon density of states of Li_6PS_5Br. The gray area represents the total phonon DOS. The corresponding plot for Li_6PS_5Cl can be found in the SI (Figure S19a).

Despite the shortcoming of not capturing microstructural effects, given the similarity of phonon DOS between crystalline and amorphous samples reported before[61,62] and found here between samples of different coherence length, the lattice dynamics calculations can be used as a proxy for both the high- and low-coherent samples. Atom projections of the phonon DOS reveal vibrations of lithium and sulfur ions throughout the entire frequency range, whereas the halide and phosphorous ions contribute to the DOS in a much narrower frequency range. These contributions are located at vastly different frequencies though. Vibrations of P^{5+} ions are located almost exclusively at the upper end of the frequency spectrum and overlap only with the DOS of PS_4^{3-}-bonded sulfur ions, suggesting almost exclusively vibrations of PS_4^{3-} tetrahedra (Figure 4c and S19a).[59] In contrast, the halide ions, Cl^- and Br^-, are coordinated by comparably large cages of Li^+ ions, in contrast to the much smaller PS_4^{3-} tetrahedra. Since the vibrational frequency scales with the square root of the force constant divided by the atomic mass, this much softer bonding environment, associated with low force constants, and the higher mass in case of bromide, cause the halide vibrations to be found in the low frequency region.

These differences in site-projected phonon DOS translate to vastly different average vibrational frequencies, occasionally also referred to as phonon band centers.[63] Average vibrational frequencies of a compound and the species therein serve as an indicator of the “softness” of the material and its respective sublattices. Lower average vibrational frequencies are often associated with enhanced ionic conductivity, as they correlate with reduced energy barriers for ion migration. Accordingly, lattice softening is a commonly pursued strategy to improve ion transport properties.[59,64] Here, the average frequencies in both materials and their respective elements are found to be almost identical (Figure 5c). The difference of vibrational frequency between both halide ions can be explained almost entirely by their mass difference. Given these similarities between argyrodites with different halides, it can be assumed that the phonon DOS of Li_6PS_5Cl is a good approximation for the phonon DOS of $Li_{5.5}PS_{4.5}Cl_{1.5}$. High charge and tight coordination environment within the PS_4^{3-} tetrahedra, cause phosphorous to exhibit the highest average frequencies of 12.1 THz. Despite being bonded to the relatively stiff PS_4^{3-} tetrahedra, the average frequencies of the sulfide ions forming PS_4^{3-} tetrahedra is only slightly above those of the “free” sulfide ion (6.1 THz and 7.0 THz, respectively). Because the frequency scales with the force constant, low frequencies correspond to high thermal displacements and indicate loose bonding. Taking the low mass of lithium into account, the average lithium-ion frequencies, which are only slightly above average compared to the total material, suggest below-average bond strengths.[59] Based on neutron powder diffraction data in this study and in literature[9], Li^+ ions were found to occupy multiple sites (T2 and T5 in Li_6PS_5Cl and T2, T5, and T5a in Li_6PS_5Br). However, during relaxation all lithium ions were found to relax onto T5 positions. As these DFT calculations are performed at 0 K, this relaxation behavior aligns with experimental observations made here and in literature[9], which found higher occupations of the T5 site at low temperatures, i.e. the T5 site is energetically slightly favored over the T2 and T5a sites. Each T5 position is coordinated by one halide, one “free” sulfide, and two PS_4^{3-}-bonded sulfide sites (Figure 5d and S19b). This tetrahedron is face-sharing with another T5 tetrahedron and two T2 tetrahedra (Figure 1b). The calculated phonon DOS cannot only be projected on individual sites but also in specific directions. To do so, contributions of phonon modes are weighted by the length of the projection of the site- and mode-specific eigenvector on the projection vector.[38] Eigenvectors orthogonal to the direction of projection are therefore neglected, whereas eigenvectors parallel to projection vector possess high weighting factors (compare Figure 5a and b). Projecting the phonon DOS in the direction of the neighboring lithium ion sites, i.e., in the direction of ionic transport reveals a significantly reduced average vibrational frequency, predominantly for the T5-T5 jump (Figure 5c). Low force constants towards the adjacent T5 site correspond to a shallow potential and high thermal displacement parameters, consistent with experimental reports which find Li^+ occupancy at the bottleneck of the T5-T5 position for the bromide argyrodite indicative of a low energy barrier for this jump. This low activation barrier was also confirmed via nudged elastic band calculations on Li_6PS_5Cl.[65]

The radial distribution of average vibrational frequencies not only holds information on the average frequency in jump-direction, but in every spatial direction (Figure 5e and S19c). Due to the loss of symmetry while ordering the primitive unit cell, each of the six Li^+ ions within the primitive unit cell, faces a slightly different local environment, leading to a slightly different radial frequency distribution. Figure 5e and S19c are therefore only chosen representative for the six individual positions. Irrespective of the halide ion in the structure, they all have in common that the central Li^+ ion is located only slightly out of the plane formed by the adjacent Li^+ sites. Regions of low average vibrational frequency are found predominantly along that plane, especially towards the T5 position, whereas regions of high frequency are rather found perpendicular to that plane. These low frequencies in jump direction result in high thermal displacement parameters, typically indicative of fast ionic conductors. The deviations between harmonic and anharmonic potentials increase with enhanced displacements from the equilibrium position. Hence, the low frequencies in jump-direction found herein suggest a strongly anharmonic, shallow potential energy landscape, corroborating findings by Ding et al.[14], who have shown that such a potential energy landscape leads to liquid-like ion dynamics and ultimately a non-zero DOS at zero-frequency at elevated temperatures (see schematic Figure 1c) in lithium argyrodites.

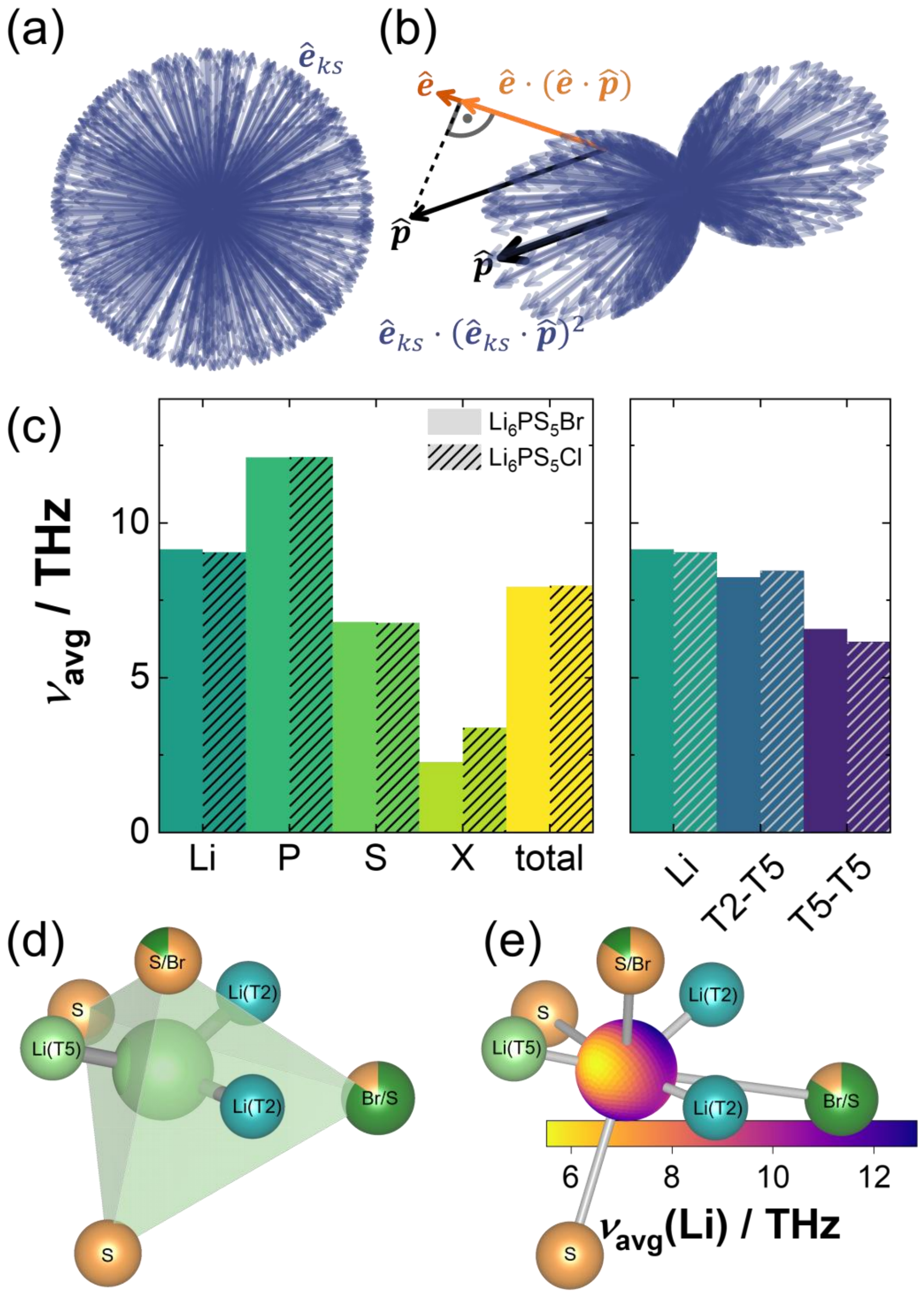

Figure 5. (a) Exemplary distribution of eigenvectors $\hat{\mathbf{e}}$ when not projected in a specific direction. Each eigenvector is a function of the q-point k and the branch index s. (b) Effect of projecting the phonon DOS along the direction $\hat{\mathbf{p}}$, both over all eigenvectors and, in more detail, for a single selected eigenvector. For visual clarity all eigenvectors are normalized to unit vectors. (c) Average atom-projected vibrational

frequencies of Li_6PS_5Br and Li_6PS_5Cl. X denotes the respective halide ion. (d) Coordination environment of the T5 site in Li_6PS_5Br. (e) Distribution of average frequencies in all spatial direction. The orientation is the same as in panel (d). A respective plot for Li_6PS_5Cl can be found in the SI (Figure S19).

Effect of coherence length on thermal conductivity

Despite the overall similarity in phonon DOS found for pristine samples and those with reduced coherence length and increased disorder, the thermal conductivity can still vary between these materials. Especially at low temperatures reduced crystallite sizes and increased disorder can function as defects at which phonon gas like phonons can get scattered.[25] Therefore, investigating thermal transport at cryogenic temperatures is paramount to assess potential changes in the thermal transport of both argyrodites with respect to their coherence length. At high temperatures, the shift from Debye-type to liquid-like lattice dynamics[14], holds the potential to dominate the magnitude and temperature dependence of thermal transport. Different ion mobilities may influence this transition and thus the thermal conductivity. Samples of Li_6PS_5Br and $Li_{5.5}PS_{4.5}Cl_{1.5}$ were measured over a temperature range of 2 K to 350 K (Figure 6). The maximum temperature was set at 350 K, as the broadening of the reflections (Figure S7) and with that effects of the post-synthesis processing were found to anneal out at temperatures as low as 373 K. Across the entire temperature range studied, low thermal conductivities were observed. Above 100 K, the thermal conductivity remains nearly constant, reflecting strong diffuson contributions at higher temperatures. This behavior is consistent with previous findings that report a flat thermal conductivity profile for argyrodites extending beyond 350 K.[66] At low temperatures, no distinct peak in thermal conductivity is observed; instead, the thermal conductivity increases sharply below 50 K before flattening out. Below 5 K, thermal conductivities scale approximately with T^2, typically for dominant grain-boundary scattering in polycrystalline materials.[67] A subtle trend may be discernible in which the reduced coherence lengths leads to a diminished increase in thermal conductivity with rising temperature. To approximate the contribution of each type of thermal transport, an analytical two-channel model is applied to the samples with lowest coherence length (right panels Figure 6, for details see Section S7).[28] This model successfully reproduces the experimentally measured thermal conductivities and demonstrates that neither purely diffuson-like nor phonon gas-like transport alone can fully account for the observed thermal transport behavior at low temperatures. Instead, thermal transport in the cryogenic regime seems to be primarily governed by phonon gas-like transport. At temperatures above ≈140 K diffuson-like conduction begins to dominate. The pronounced anharmonicity of lattice vibrations in argyrodites demonstrated here and by Ding et al.[14] as well as the liquid-like dynamics of lithium ions at higher temperatures, accompanied by a breakdown of the Debye-type phonon DOS, disrupts phonon propagation and is believed to enhance phonon linewidth. Although the transition to liquid-like dynamics occurs around 400 K, its influence extends into the temperature range over which thermal conductivity was measured (up to 350 K).[14] These factors contribute to the dominance of diffuson-type and the low magnitude of thermal transport at elevated temperatures.[22,68] Additionally, these findings may also explain the observed reduction in the sharpness of the conductivity increase in samples with reduced coherence lengths. Enhanced disorder, smaller crystallites, and the introduction of strain can function as additional defect sites that scatter phonons, increasing resistance to heat transport and reducing phonon gas-type thermal conductivity. In contrast, structural effects such as anion disorder and strain might be expected to enhance diffuson-type transport: Variations in the local coordination environment of atoms change the (local) frequency of vibrations, which broadens the phonon linewidth and thereby increases diffuson-type thermal transport. However, the minor changes observed in the pair distribution function, primarily affecting the second and higher coordination spheres, indicate that the associated increase in vibrational disorder may be insufficient to enhance diffuson transport within the sensitivity limits of the measurements. Overall, no strong influence of the coherence length on the thermal transport is found further corroborating the dominance of local vibrations and anharmonicity on the transport.

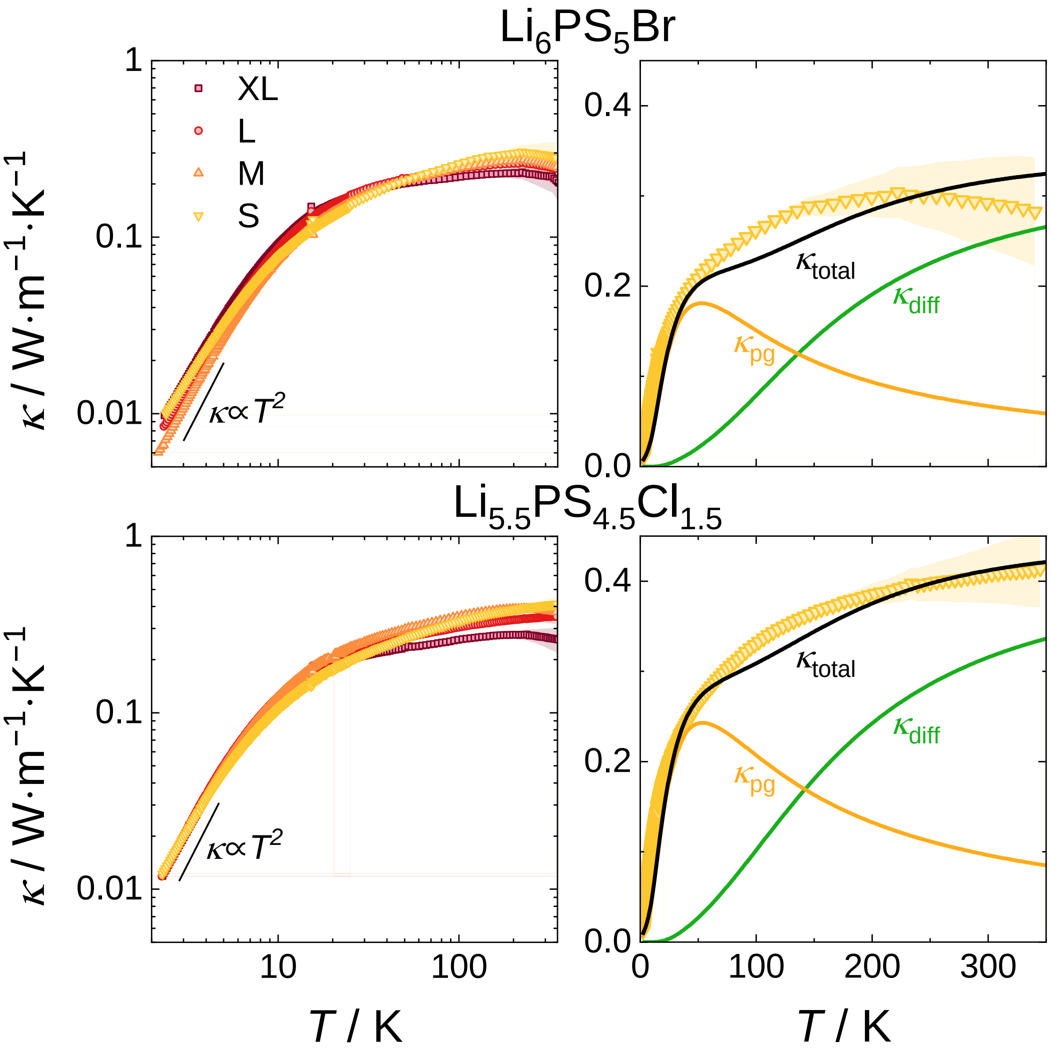

Figure 6. Thermal conductivities of Li_6PS_5Br and $Li_{5.5}PS_{4.5}Cl_{1.5}$ processed with different coherence lengths. At the lowest temperatures, below 5 K, thermal conductivities scale with approximately with T^2 (left panels). The samples with lowest coherence length were fitted using an analytical two-channel model. At low temperatures significant phonon gas contributions were found (right panels).

Effect of structural disorder on thermal conductivity

While the effect of coherence length on thermal conductivity is found to be rather minor, previous reports of the thermal conductivity on substitution series of solid electrolytes[22,28] have demonstrated much more significant changes upon structural ordering. Typically, phonon peaks are observed for fully ordered endmembers and a suppression of such within the substitution series is found.[28] In the family of lithium argyrodites, the iodine argyrodite Li_6PS_5I exhibits even at room temperature a fully anion ordered host lattice due to the significant size mismatch between sulfur and iodine ions, which suppresses site disorder.[9] Upon cooling, Li_6PS_5I undergoes a phase transition to a fully ordered monoclinic phase (*Cc*, space group no. 9).[69] Within the $Li_6PS_5Br_xI_{1-x}$ substitution series, partial substitution of iodine by bromine progressively introduces structural Br^-/I^- and potentially Br^-/S^{2-} disorder into the host lattice, making it optimally suited to investigate the effect of structural disorder on the thermal conductivity in lithium argyrodites. Neutron and X-ray powder diffraction are used to determine the presence of a phase transition and, in case of a phase transition, the structure of the low temperature polymorph as well as the phase transition temperature. Li_6PS_5I, $Li_6PS_5Br_{0.1}I_{0.9}$, and $Li_6PS_5Br_{0.2}I_{0.8}$ all exhibit a phase transition to a monoclinic phase. The phase transitions stretch over a certain temperature range, which gets wider and shifts to lower onset temperatures as the bromine content increases (Figures S20 to S24). Similar phase transitions in Li_6PS_5Br, Li_6PS_5Cl, and $Li_{5.5}PS_{4.5}Cl_{1.5}$ were ruled out via neutron powder diffraction down to 5 K (Figures S25-S28). A more detailed discussion on the low-temperature structure characterization can be found in the Supporting Information (Section S8).

The increasing disorder within the $Li_6PS_5Br_xI_{1-x}$ may disrupt the flow of thermal energy, as mass contrast and radius difference between bromide and iodide ions introduces point defect scattering sites (Figure 7a and b). Consistent with this hypothesis, a systematic reduction in thermal conductivity is observed with increasing bromine content across all measured temperatures (Figure 7c). For both Li_6PS_5I and $Li_6PS_5Br_{0.1}I_{0.9}$ a distinct phonon peak below the phase transition can be observed. In contrast, in $Li_6PS_5Br_{0.2}I_{0.8}$ only a very shallow maximum is found and its thermal conductivity remains essentially temperature-independent above 50 K. At temperatures above 170 K, Li_6PS_5I and $Li_6PS_5Br_{0.1}I_{0.9}$ exhibit a slightly increase in thermal conductivity, which is in line with previously reported values on Li_6PS_5I up to 573 K obtained via laser flash analysis.[66] The complete suppression of the phonon peak upon 20% bromine substitution underscores the sensitivity of low-temperature thermal transport towards structural disorder in lithium argyrodites and potentially in solid electrolytes in general.

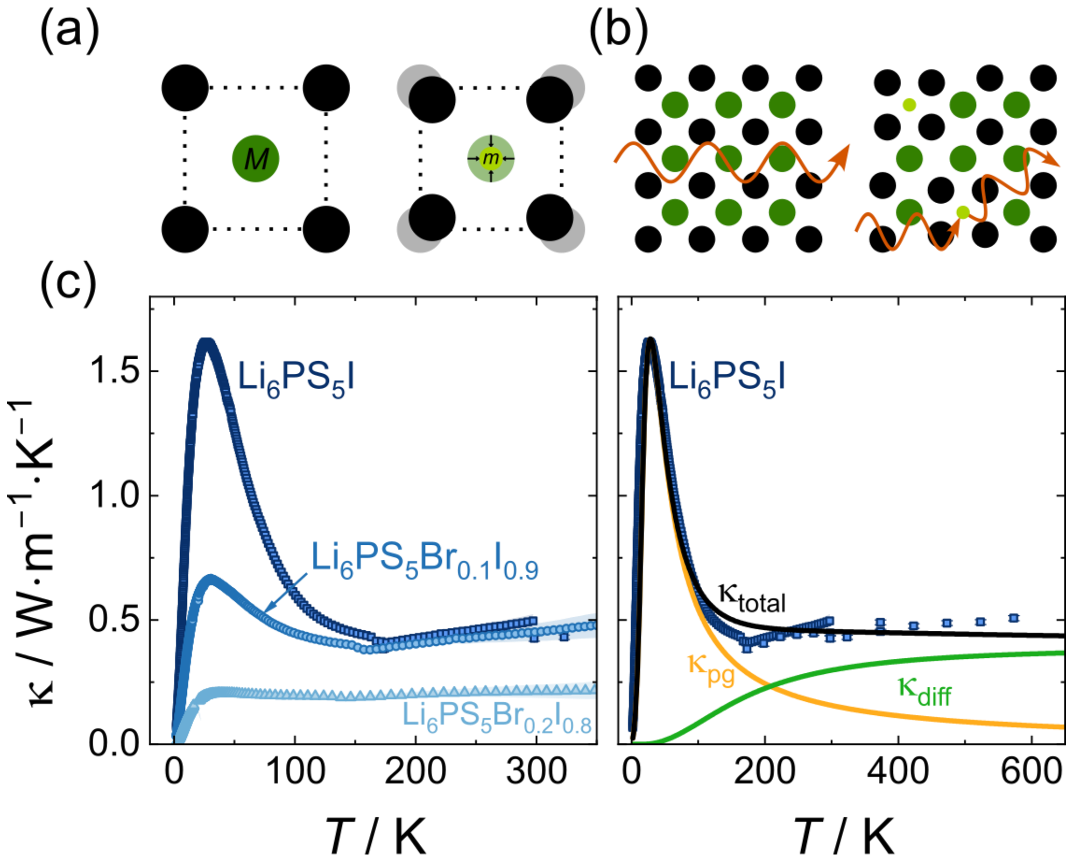

Figure 7. (a) The substitution of an iodide ion (dark green) with a smaller, lighter bromide ion (light green) introduces a mass and size contrast and causes the lattice to shrink locally. (b) These lattice perturbations allow phonons, depicted in orange, to exhibit enhanced phonon scattering. (c) Left panel: Influence of the loss of structural order on the thermal conductivity, drastically reducing and ultimately suppressing the phonon peak. Right panel: Fit of an analytical two-channel model to the experimental thermal conductivity of Li_6PS_5I*. High-temperature thermal conductivity data was taken from literature*[66]*.*

The pronounced difference between the impact of reduced coherence length and the effect of structural disorder on low-temperature thermal conductivity (compare Figure 6 and Figure 7) can be rationalized by their characteristic length scales. While the coherence length is in the order of 10^1 nm, structural disorder acts in the range of 10^{-1} nm to 10^0 nm. The latter provides a much higher density of defect sites for the phonon gas-type phonons to be scattered on. Consequently, only in well-ordered systems, like monoclinic Li_6PS_5I, phonons are able to propagate significant distances, allowing for the observation of a phonon peak.

A detailed understanding of the temperature dependence of thermal conductivity, the relative contributions of phonon gas and diffuson-like transport, the effects of liquid-like ion dynamics, anharmonic potential energy landscapes, and coherence loss is essential for rationally engineering solid electrolytes. These factors govern how thermal energy is transported through the disordered and often dynamically fluctuating ionic frameworks of such materials. Insights into these mechanisms enable the targeted tuning of lattice thermal conductivity, e.g., to manage heat dissipation in commercialized applications, thereby supporting the development of solid electrolytes with optimized transport properties and their processing procedures. However, the findings of this study imply that enhancing diffuson-type transport may require fundamentally different structural engineering strategies.

Conclusion

This work demonstrates that post-synthesis processing procedures markedly alter crystallite size and strain, and thereby also coherence length. These changes have concurrent effects on the ionic transport in lithium argyrodites. While for moderate mechanical energy input, an increase in ionic conductivity is found, more severe treatments reduce ionic conductivity by disrupting the percolating Li^+ diffusion network, despite a nearly unchanged activation energy. In contrast, the effect of reduced coherence length on vibrational frequencies and thermal conductivity was found to be comparably small, suggesting that phonon mean free paths are already suppressed below the length scale of the coherence length. Instead, the effect of structural disorder is much more significant in reducing thermal conductivity through enhanced point defect scattering. The predominance of diffuson-type heat conduction, alongside a phonon gas contribution at cryogenic temperatures was confirmed with an analytical two-channel model successfully decomposing these channels. These dominant diffuson contributions, indicate high phonon linewidths, and thus very anharmonic lattice dynamics. Radial frequency distributions on the lithium ion sites further support the picture of a shallow potential energy surface with strong anharmonic contributions previously reported by Ding et al.[14] for Li_6PS_5Cl. Collectively, these findings underscore the delicate balance between structural coherence, disorder, ion dynamics, local lattice dynamics, and heat transport in solid electrolytes. They emphasize the importance for the optimization of mechanical treatment protocols to maximize ionic conductivities. In contrast, the thermal conductivity is mainly unaffected by such treatments, potentially shifting the major part of engineering temperature control in such solid-state batteries towards an external thermal management system instead of the solid electrolyte.

Supporting Information

Computational parameters, refinements of total scattering analysis, analysis of amorphous content, Nyquist plots, Raman spectroscopy, additional plots on QENS, activation energies found with NMR, additional plots on lattice dynamics, analytical two-channel model, low-temperature X-ray and neutron diffraction.

Notes

The authors declare no competing financial interest.

Data availability statement.

All data of this study are available in datastore. by Universität Münster under the DOI 10.17879/02978575924. Raw data of neutron scattering experiments conducted at ORNL are available under the DOI 10.14461/oncat.data/2572XXX. Raw data of white beam normalization data used for the ARCS and POWGEN experiments are available under the DOIs 10.14461/oncat.data/2570733, and 10.14461/oncat.data/2571204, respectively. Proposal and experimental report of the beamtime conducted at D2B are available under the DOI 10.5291/ILL-DATA.5-22-824.

Acknowledgments

This study is funded by the European Union (ERC, DIONISOS, 101123802). Views and opinions expressed are however those of the author(s) only and do not necessarily reflect those of the European Union or the European Research Council Executive Agency. Neither the European Union nor the granting authority can be held responsible for them. The research was supported by the International Graduate School for Battery Chemistry, Characterization, Analysis, Recycling and Application (BACCARA), which is funded by the Ministry for Culture and Science of North Rhine Westphalia, Germany. The simulations for this work were performed on the computer cluster PALMA II of the University of Münster. The authors further acknowledge funding from the Deutsche Forschungsgemeinschaft under project number 459785385. This research used resources at the Spallation Neutron Source, a DOE Office of Science User Facility operated by the Oak Ridge National Laboratory. The beam time was allocated to BASIS, ARCS, and POWGEN on proposal numbers IPTS-32496, IPTS-32542, and IPTS-34157, respectively. The authors acknowledge Institut Laue-Langevin for time on the D2B beamline under the proposal 5-22-824. Additionally, the authors thank Alexander Sobolev, Martin Lange, and Bianca Helm for assistance at Institut Laue-Langevin.

References

(1) Janek, J.; Zeier, W. G. Challenges in speeding up solid-state battery development. *Nat. Energy* **2023**, *8* (3), 230–240. DOI: 10.1038/s41560-023-01208-9.

(2) Janek, J.; Zeier, W. G. A solid future for battery development. *Nat. Energy* **2016**, *1* (9), 16141. DOI: 10.1038/nenergy.2016.141.

(3) Jung, K.-N.; Shin, H.-S.; Park, M.-S.; Lee, J.-W. Solid-State Lithium Batteries: Bipolar Design, Fabrication, and Electrochemistry. *ChemElectroChem* **2019**, *6* (15), 3842–3859. DOI: 10.1002/celc.201900736.

(4) Lewis, J. A.; Cavallaro, K. A.; Liu, Y.; McDowell, M. T. The promise of alloy anodes for solid-state batteries. *Joule* **2022**, *6* (7), 1418–1430. DOI: 10.1016/j.joule.2022.05.016.

(5) Krauskopf, T.; Richter, F. H.; Zeier, W. G.; Janek, J. Physicochemical Concepts of the Lithium Metal Anode in Solid-State Batteries. *Chem. Rev.* **2020**, *120* (15), 7745–7794. DOI: 10.1021/acs.chemrev.0c00431. Published Online: Jul. 27, 2020.

(6) Hatzell, K. B.; Chen, X. C.; Cobb, C. L.; Dasgupta, N. P.; Dixit, M. B.; Marbella, L. E.; McDowell, M. T.; Mukherjee, P. P.; Verma, A.; Viswanathan, V.; Westover, A. S.; Zeier, W. G. Challenges in Lithium Metal Anodes for Solid-State Batteries. *ACS Energy Lett.* **2020**, *5* (3), 922–934. DOI: 10.1021/acsenergylett.9b02668.

(7) Famprikis, T.; Canepa, P.; Dawson, J. A.; Islam, M. S.; Masquelier, C. Fundamentals of inorganic solid-state electrolytes for batteries. *Nat. Mater.* **2019**, *18* (12), 1278–1291. DOI: 10.1038/s41563-019-0431-3. Published Online: Aug. 19, 2019.

(8) Zhou, L.; Minafra, N.; Zeier, W. G.; Nazar, L. F. Innovative Approaches to Li-Argyrodite Solid Electrolytes for All-Solid-State Lithium Batteries. *Acc. Chem. Res.* **2021**, *54* (12), 2717–2728. DOI: 10.1021/acs.accounts.0c00874. Published Online: May. 25, 2021.

(9) Minafra, N.; Kraft, M. A.; Bernges, T.; Li, C.; Schlem, R.; Morgan, B. J.; Zeier, W. G. Local Charge Inhomogeneity and Lithium Distribution in the Superionic Argyrodites Li6PS5X (X = Cl, Br, I). *Inorg. Chem.* **2020**, *59* (15), 11009–11019. DOI: 10.1021/acs.inorgchem.0c01504.

(10) Gautam, A.; Sadowski, M.; Ghidiu, M.; Minafra, N.; Senyshyn, A.; Albe, K.; Zeier, W. G. Engineering the Site-Disorder and Lithium Distribution in the Lithium Superionic Argyrodite Li6PS5Br. *Adv. Energy Mater.* **2021**, *11* (5), 2003369. DOI: 10.1002/aenm.202003369.

(11) Gautam, A.; Ghidiu, M.; Suard, E.; Kraft, M. A.; Zeier, W. G. On the Lithium Distribution in Halide Superionic Argyrodites by Halide Incorporation in Li7-xPS6-xClx. *ACS Appl. Energy Mater.* **2021**, *4* (7), 7309–7315. DOI: 10.1021/acsaem.1c01417.

(12) Adeli, P.; Bazak, J. D.; Park, K. H.; Kochetkov, I.; Huq, A.; Goward, G. R.; Nazar, L. F. Boosting Solid-State Diffusivity and Conductivity in Lithium Superionic Argyrodites by Halide Substitution. *Angew. Chem. Int. Ed. Engl.* **2019**, *58* (26), 8681–8686. DOI: 10.1002/anie.201814222. Published Online: May. 24, 2019.

(13) Li, S.; Lin, J.; Schaller, M.; Indris, S.; Zhang, X.; Brezesinski, T.; Nan, C.-W.; Wang, S.; Strauss, F. High-Entropy Lithium Argyrodite Solid Electrolytes Enabling Stable All-Solid-State Batteries. *Angew. Chem. Int. Ed. Engl.* **2023**, *62* (50), e202314155. DOI: 10.1002/anie.202314155. Published Online: Nov. 13, 2023.

(14) Ding, J.; Gupta, M. K.; Rosenbach, C.; Lin, H.-M.; Osti, N. C.; Abernathy, D. L.; Zeier, W. G.; Delaire, O. Liquid-like dynamics in a solid-state lithium electrolyte. *Nat. Phys.* **2025**, *21* (1), 118–125. DOI: 10.1038/s41567-024-02707-6.

(15) Zhao, T.; Sobolev, A. N.; Schlem, R.; Helm, B.; Kraft, M. A.; Zeier, W. G. Synthesis-Controlled Cation Solubility in Solid Sodium Ion Conductors Na2+xZr1–xInxCl6. *ACS Appl. Energy Mater.* **2023**, *6* (8), 4334–4341. DOI: 10.1021/acsaem.3c00277.

(16) Schlautmann, E.; Weiß, A.; Maus, O.; Ketter, L.; Rana, M.; Puls, S.; Nickel, V.; Gabbey, C.; Hartnig, C.; Bielefeld, A.; Zeier, W. G. Impact of the Solid Electrolyte Particle Size Distribution in Sulfide-Based Solid-State Battery Composites. *Adv. Energy Mater.* **2023**, *13* (41). DOI: 10.1002/aenm.202302309.

(17) Wang, Y.; Hao, H.; Naik, K. G.; Vishnugopi, B. S.; Fincher, C. D.; Yan, Q.; Raj, V.; Celio, H.; Yang, G.; Fang, H.; Chiang, Y.-M.; Perras, F. A.; Jena, P.; Watt, J.; Mukherjee, P. P.; Mitlin, D. Mechanical Milling – Induced Microstructure Changes in Argyrodite LPSCl Solid-State Electrolyte Critically Affect Electrochemical Stability. *Adv. Energy Mater.* **2024**, *14* (23). DOI: 10.1002/aenm.202304530.

(18) Maus, O.; Lange, M. A.; Frankenberg, F.; Stainer, F.; Faka, V.; Schlautmann, E.; Rosenbach, C.; Jodlbauer, A.; Schubert, J.; Janek, J.; Li, C.; Michalowski, P.; Wilkening, H. M. R.; Kwade, A.; Zeier, W. G. Influence of Post-Synthesis Processing on the Structure, Transport, and Performance of the Solid Electrolyte Li 5.5 PS 4.5 Cl 1.5 in All-Solid-State Batteries. *Adv. Energy Mater.* **2025**, *15* (5), 2403291. DOI: 10.1002/aenm.202403291. Published Online: Sep. 5, 2024.

(19) Schweiger, L.; Hogrefe, K.; Gadermaier, B.; Rupp, J. L. M.; Wilkening, H. M. R. Ionic Conductivity of Nanocrystalline and Amorphous Li10GeP2S12: The Detrimental Impact of Local Disorder on Ion Transport. *J. Am. Chem. Soc.* **2022**, *144* (22), 9597–9609. DOI: 10.1021/jacs.1c13477. Published Online: May. 24, 2022.

(20) Kim, T.; Chang, H.; Song, G.; Lee, S.; Kim, K.; Lee, S.; Moon, J.; Lee, K. T. Critical Factors Contributing to the Thermal Runaway of Thiophosphate Solid Electrolytes for All-Solid-State Batteries. *Adv. Funct. Mater.* **2024**, *34* (42), 2404806. DOI: 10.1002/adfm.202404806.

(21) Yoon, K.; Kim, H.; Han, S.; Chan, T.-S.; Ko, K.-H.; Jo, S.; Park, J.; Kim, S.; Lee, S.; Noh, J.; Kim, W.; Lim, J.; Kang, K. Detrimental effect of high-temperature storage on sulfide-based all-solid-state batteries. *Applied Physics Reviews* **2022**, *9* (3). DOI: 10.1063/5.0088838.

(22) Böger, T.; Bernges, T.; Agne, M. T.; Canepa, P.; Tietz, F.; Zeier, W. G. On the Thermal Conductivity and Local Lattice Dynamical Properties of NASICON Solid Electrolytes. *J. Am. Chem. Soc.* **2024**, *146* (47), 32678–32688. DOI: 10.1021/jacs.4c12034. Published Online: Nov. 13, 2024.

(23) Gupta, M. K.; Ding, J.; Bansal, D.; Abernathy, D. L.; Ehlers, G.; Osti, N. C.; Zeier, W. G.; Delaire, O. Strongly Anharmonic Phonons and Their Role in Superionic Diffusion and Ultralow Thermal Conductivity of Cu7PSe6. *Adv. Energy Mater.* **2022**, *12* (23), 2200596. DOI: 10.1002/aenm.202200596.

(24) Bernges, T.; Böger, T.; Maus, O.; Till, P. S.; Agne, M. T.; Zeier, W. G. Scaling Relations for Ionic and Thermal Transport in the Na+ Ionic Conductor Na3PS4. *ACS Materials Lett.* **2022**, *4* (12), 2491–2498. DOI: 10.1021/acsmaterialslett.2c00846.

(25) Hunklinger, S.; Enss, C., Eds. *Solid State Physics*; De Gruyter, 2022. DOI: 10.1515/9783110666502.

(26) Allen, P. B.; Feldman, J. L.; Fabian, J.; Wooten, F. Diffusons, locons and propagons: Character of atomic vibrations in amorphous Si. *Philos. Mag. B* **1999**, *79* (11-12), 1715–1731. DOI: 10.1080/13642819908223054.

(27) Acharyya, P.; Ghosh, T.; Pal, K.; Rana, K. S.; Dutta, M.; Swain, D.; Etter, M.; Soni, A.; Waghmare, U. V.; Biswas, K. Glassy thermal conductivity in Cs3Bi2I6Cl3 single crystal. *Nat. Commun.* **2022**, *13* (1), 5053. DOI: 10.1038/s41467-022-32773-4. Published Online: Aug. 27, 2022.

(28) Bernges, T.; Peterlechner, M.; Wilde, G.; Agne, M. T.; Zeier, W. G. Analytical model for two-channel phonon transport engineering. *Mater. Today Phys.* **2023**, *35*, 101107. DOI: 10.1016/j.mtphys.2023.101107.

(29) Hanus, R. C.; George, J.; Wood, M.; Bonkowski, A.; Cheng, Y.; Abernathy, D. L.; Manley, M. E.; Hautier, G.; Snyder, G. J.; Hermann, R. P. Uncovering design principles for amorphous-like heat conduction using two-channel lattice dynamics. *Mater. Today Phys.* **2021**, *18*, 100344. DOI: 10.1016/j.mtphys.2021.100344.

(30) Simoncelli, M.; Marzari, N.; Mauri, F. Unified theory of thermal transport in crystals and glasses. *Nat. Phys.* **2019**, *15* (8), 809–813. DOI: 10.1038/s41567-019-0520-x.

(31) Togo, A.; Shinohara, K.; Tanaka, I. Spglib: a software library for crystal symmetry search. *Sci. Technol. Adv. Mater. Methods* **2024**, *4* (1). DOI: 10.1080/27660400.2024.2384822.

(32) Kresse; Furthmüller. Efficient iterative schemes for ab initio total-energy calculations using a plane-wave basis set. *Phys. Rev. B: Condens. Matter* **1996**, *54* (16), 11169–11186. DOI: 10.1103/physrevb.54.11169.

(33) Kresse, G.; Furthmüller, J. Efficiency of ab-initio total energy calculations for metals and semiconductors using a plane-wave basis set. *Comput. Mater. Sci.* **1996**, *6* (1), 15–50. DOI: 10.1016/0927-0256(96)00008-0.

(34) Kresse, G.; Joubert, D. From ultrasoft pseudopotentials to the projector augmented-wave method. *Phys. Rev. B* **1999**, *59* (3), 1758–1775. DOI: 10.1103/PhysRevB.59.1758.

(35) Blöchl, P. E. Projector augmented-wave method. *Phys. Rev. B: Condens. Matter* **1994**, *50* (24), 17953–17979. DOI: 10.1103/PhysRevB.50.17953.

(36) Perdew, J. P.; Ruzsinszky, A.; Csonka, G. I.; Vydrov, O. A.; Scuseria, G. E.; Constantin, L. A.; Zhou, X.; Burke, K. Restoring the density-gradient expansion for exchange in solids and surfaces. *Phys. Rev. Lett.* **2008**, *100* (13), 136406. DOI: 10.1103/PhysRevLett.100.136406. Published Online: Apr. 4, 2008.

(37) Togo, A.; Chaput, L.; Tanaka, I. Distributions of phonon lifetimes in Brillouin zones. *Phys. Rev. B* **2015**, *91* (9), 94306. DOI: 10.1103/PhysRevB.91.094306.

(38) Togo, A.; Tanaka, I. First principles phonon calculations in materials science. *Scr. Mater.* **2015**, *108*, 1–5. DOI: 10.1016/j.scriptamat.2015.07.021.

(39) Williamson, G.; Hall, W. X-ray line broadening from filed aluminium and wolfram. *Acta Metall.* **1953**, *1* (1), 22–31. DOI: 10.1016/0001-6160(53)90006-6.

(40) Faka, V.; Agne, M. T.; Lange, M. A.; Daisenberger, D.; Wankmiller, B.; Schwarzmüller, S.; Huppertz, H.; Maus, O.; Helm, B.; Böger, T.; Hartel, J.; Gerdes, J. M.; Molaison, J. J.; Kieslich, G.; Hansen, M. R.; Zeier, W. G. Pressure-Induced Dislocations and Their Influence on Ionic Transport in Li+-Conducting Argyrodites. *J. Am. Chem. Soc.* **2024**, *146* (2), 1710–1721. DOI: 10.1021/jacs.3c12323. Published Online: Jan. 4, 2024.

(41) Thomae, S. L. J.; Prinz, N.; Hartmann, T.; Teck, M.; Correll, S.; Zobel, M. Pushing data quality for laboratory pair distribution function experiments. *Rev. Sci. Instrum.* **2019**, *90* (4), 43905. DOI: 10.1063/1.5093714.

(42) Juhás, P.; Davis, T.; Farrow, C. L.; Billinge, S. J. L. PDFgetX3 : a rapid and highly automatable program for processing powder diffraction data into total scattering pair distribution functions. *J. Appl. Crystallogr.* **2013**, *46* (2), 560–566. DOI: 10.1107/S0021889813005190.

(43) Coelho, A. A. TOPAS and TOPAS-Academic: an optimization program integrating computer algebra and crystallographic objects written in C++. *J. Appl. Crystallogr.* **2018**, *51* (1), 210–218. DOI: 10.1107/S1600576718000183.

(44) Mamontov, E.; Herwig, K. W. A time-of-flight backscattering spectrometer at the Spallation Neutron Source, BASIS. *Rev. Sci. Instrum.* **2011**, *82* (8), 85109. DOI: 10.1063/1.3626214.

(45) Arnold, O.; Bilheux, J. C.; Borreguero, J. M.; Buts, A.; Campbell, S. I.; Chapon, L.; Doucet, M.; Draper, N.; Ferraz Leal, R.; Gigg, M. A.; Lynch, V. E.; Markvardsen, A.; Mikkelson, D. J.; Mikkelson, R. L.; Miller, R.; Palmen, K.; Parker, P.; Passos, G.; Perring, T. G.; Peterson, P. F.; Ren, S.; Reuter, M. A.; Savici, A. T.; Taylor, J. W.; Taylor, R. J.; Tolchenov, R.; Zhou, W.; Zikovsky, J. Mantid—Data analysis and visualization package for neutron scattering and μ SR experiments. *Nucl. Instrum. Methods Phys. Res., Sect. A* **2014**, *764*, 156–166. DOI: 10.1016/j.nima.2014.07.029.

(46) Azuah, R. T.; Kneller, L. R.; Qiu, Y.; Tregenna-Piggott, P. L. W.; Brown, C. M.; Copley, J. R. D.; Dimeo, R. M. DAVE: A Comprehensive Software Suite for the Reduction, Visualization, and Analysis of Low Energy Neutron Spectroscopic Data. *Journal of Research of the National Institute of Standards and Technology* **2009**, *114* (6), 341–358. DOI: 10.6028/jres.114.025. Published Online: Dec. 1, 2009.

(47) Chudley, C. T.; Elliott, R. J. Neutron Scattering from a Liquid on a Jump Diffusion Model. *Proc. Phys. Soc.* **1961**, *77* (2), 353–361. DOI: 10.1088/0370-1328/77/2/319.

(48) Abernathy, D. L.; Stone, M. B.; Loguillo, M. J.; Lucas, M. S.; Delaire, O.; Tang, X.; Lin, J. Y. Y.; Fultz, B. Design and operation of the wide angular-range chopper spectrometer ARCS at the Spallation Neutron Source. *Rev. Sci. Instrum.* **2012**, *83* (1), 15114. DOI: 10.1063/1.3680104.

(49) Y. Y. Lin, J.; Islam, F.; Kresh, M. Multiphonon: Phonon Density of States tools for Inelastic Neutron Scattering Powder Data. *J. Open Source Softw.* **2018**, *3* (21), 440. DOI: 10.21105/joss.00440.

(50) Huq, A.; Kirkham, M.; Peterson, P. F.; Hodges, J. P.; Whitfield, P. S.; Page, K.; Hűgle, T.; Iverson, E. B.; Parizzi, A.; Rennich, G. POWGEN: rebuild of a third-generation powder diffractometer at the Spallation Neutron Source. *J. Appl. Crystallogr.* **2019**, *52* (Pt 5), 1189–1201. DOI: 10.1107/S160057671901121X. Published Online: Oct. 1, 2019.

(51) Thompson, P.; Cox, D. E.; Hastings, J. B. Rietveld refinement of Debye–Scherrer synchrotron X-ray data from Al2O3. *J. Appl. Crystallogr.* **1987**, *20* (2), 79–83. DOI: 10.1107/S0021889887087090.

(52) Blumm, J.; Opfermann, J. Improvement of the mathematical modeling of flash measurements. *High Temp.-High Press.* **2002**, *34* (5), 515–521. DOI: 10.1068/htjr061.

(53) Cape, J. A.; Lehman, G. W. Temperature and Finite Pulse-Time Effects in the Flash Method for Measuring Thermal Diffusivity. *J. Appl. Phys.* **1963**, *34* (7), 1909–1913. DOI: 10.1063/1.1729711.

(54) Shotwell, A. M.; Schulze, M. C.; Yox, P.; Alaniz, C.; Maughan, A. E. Tetrahedral Tilting and Lithium-Ion Transport in Halide Argyrodites Prepared by Rapid, Microwave-Assisted Synthesis. *Adv. Funct. Mater.* **2025.** DOI: 10.1002/adfm.202500237.

(55) Schlenker, R.; Hansen, A.-L.; Senyshyn, A.; Zinkevich, T.; Knapp, M.; Hupfer, T.; Ehrenberg, H.; Indris, S. Structure and Diffusion Pathways in Li6PS5Cl Argyrodite from Neutron Diffraction, Pair-Distribution Function Analysis, and NMR. *Chem. Mater.* **2020**, *32* (19), 8420–8430. DOI: 10.1021/acs.chemmater.0c02418.

(56) Ketter, L.; Greb, N.; Bernges, T.; Zeier, W. G. Using resistor network models to predict the transport properties of solid-state battery composites. *Nat. Commun.* **2025**, *16* (1), 1411. DOI: 10.1038/s41467-025-56514-5. Published Online: Feb. 6, 2025.

(57) Schwaighofer, B.; Gonzalez, M. A.; Johnson, M. R.; Evans, J. S. O.; Evans, I. R. Ionic Mobility in Energy Materials: Through the Lens of Quasielastic Neutron Scattering. *Chem. Mater.* **2025**, *37* (10), 3575–3593. DOI: 10.1021/acs.chemmater.5c00238.

(58) Hogrefe, K.; Stainer, F.; Minafra, N.; Zeier, W. G.; Wilkening, H. M. R. NMR Down to Cryogenic Temperatures: Accessing the Rate-Limiting Step of Li Transport in Argyrodite Electrolytes. *Chem. Mater.* **2024**, *36* (13), 6527–6534. DOI: 10.1021/acs.chemmater.4c00746.

(59) Krauskopf, T.; Muy, S.; Culver, S. P.; Ohno, S.; Delaire, O.; Shao-Horn, Y.; Zeier, W. G. Comparing the Descriptors for Investigating the Influence of Lattice Dynamics on Ionic Transport Using the Superionic Conductor Na3PS4- xSe x. *J. Am. Chem. Soc.* **2018**, *140* (43), 14464–14473. DOI: 10.1021/jacs.8b09340. Published Online: Oct. 17, 2018.

(60) Gupta, M. K.; Ding, J.; Osti, N. C.; Abernathy, D. L.; Arnold, W.; Wang, H.; Hood, Z.; Delaire, O. Fast Na diffusion and anharmonic phonon dynamics in superionic Na3PS4. *Energy Environ. Sci.* **2021**, *14* (12), 6554–6563. DOI: 10.1039/D1EE01509E.

(61) Chen, L.; Kumari, N.; Hou, Y. Thermal resistances of crystalline and amorphous few-layer oxide thin films. *AIP Adv.* **2017**, *7* (11). DOI: 10.1063/1.5007299.

(62) Verdier, M.; Han, Y.; Lacroix, D.; Chapuis, P.-O.; Termentzidis, K. Radial dependence of thermal transport in silicon nanowires. *J. Phys. Mater.* **2019**, *2* (1), 15002. DOI: 10.1088/2515-7639/aaead5.

(63) Muy, S.; Schlem, R.; Shao-Horn, Y.; Zeier, W. G. Phonon–Ion Interactions: Designing Ion Mobility Based on Lattice Dynamics. *Adv. Energy Mater.* **2021**, *11* (15), 2002787. DOI: 10.1002/aenm.202002787.

(64) Schlem, R.; Ghidiu, M.; Culver, S. P.; Hansen, A.-L.; Zeier, W. G. Changing the Static and Dynamic Lattice Effects for the Improvement of the Ionic Transport Properties within the Argyrodite Li 6 PS 5– x Se x I. *ACS Appl. Energy Mater.* **2020**, *3* (1), 9–18. DOI: 10.1021/acsaem.9b01794.

(65) Jeon, T.; Cha, G. H.; Jung, S. C. Understanding the anion disorder governing lithium distribution and diffusion in an argyrodite Li 6 PS 5 Cl solid electrolyte. *J. Mater. Chem. A* **2024**, *12* (2), 993–1002. DOI: 10.1039/D3TA06069A.

(66) Böger, T.; Bernges, T.; Li, Y.; Canepa, P.; Zeier, W. G. Thermal Conductivities of Lithium-Ion-Conducting Solid Electrolytes. *ACS Appl. Energy Mater.* **2023**, *6* (20), 10704–10712. DOI: 10.1021/acsaem.3c01977.

(67) Hanus, R.; Garg, A.; Snyder, G. J. Phonon diffraction and dimensionality crossover in phonon-interface scattering. *Commun Phys* **2018**, *1* (1). DOI: 10.1038/s42005-018-0070-z.

(68) Krenzer, G.; Kim, C.-E.; Tolborg, K.; Morgan, B. J.; Walsh, A. Anharmonic lattice dynamics of superionic lithium nitride. *J. Mater. Chem. A* **2022**, *10* (5), 2295–2304. DOI: 10.1039/D1TA07631K.

(69) Kong, S.-T.; Deiseroth, H.-J.; Reiner, C.; Gün, O.; Neumann, E.; Ritter, C.; Zahn, D. Lithium argyrodites with phosphorus and arsenic: order and disorder of lithium atoms, crystal chemistry, and phase transitions. *Chem. Eur. J.* **2010**, *16* (7), 2198–2206. DOI: 10.1002/chem.200902470.

TOC Figure

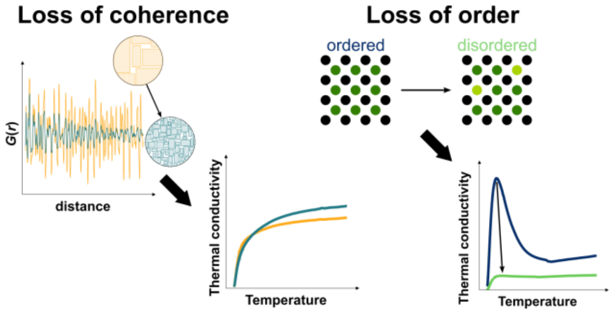

Post-synthesis treatment of lithium argyrodites reduces coherence length and crystallite size but thermal conductivity is almost. In contrast, structural disordering significantly changes thermal conductivity by suppressing phonon gas-type thermal transport.